THESIS FOR THE DEGREE OF DOCTOR OF PHILOSOPHY IN
SOLID AND STRUCTURAL MECHANICS

Process Modeling of Liquid Composite Molding Processes

DA WU

Department of Industrial and Materials Science
Division of Material and Computational Mechanics
CHALMERS UNIVERSITY OF TECHNOLOGY

Göteborg, Sweden 2020

Process Modeling of Liquid Composite Molding Processes
DA WU
ISBN 978-91-7905-285-0

© DA WU, 2020

Doktorsavhandlingar vid Chalmers tekniska högskola
Ny serie nr. 4752
ISSN 0346-718X
Department of Industrial and Materials Science
Division of Material and Computational Mechanics
Chalmers University of Technology
SE-412 96 Göteborg
Sweden
Telephone: +46 (0)31-772 1000

Cover:
Snapshot from a holistic simulation of the VARTM process at 70 seconds. The distribution of degree of saturation ξ, fluid pressure p, temperature Θ, degree of cure c, resin viscosity μ, and fiber preform deformation λ are plotted sequentially.

Chalmers Reproservice
Göteborg, Sweden 2020

Process Modeling of Liquid Composite Molding Processes
Thesis for the Degree of Doctor of Philosophy
DA WU
Department of Industrial and Materials Science
Division of Material and Computational Mechanics
Chalmers University of Technology

Abstract

The polymer matrix composites (PMCs) are carving out a niche amid the keen market competition to replace the other material counterparts, e.g., metals. Due to the low weight and the corrosion resistance, the PMCs are wildly utilized from aerospace to automobile industries, both in the sectors of civilian and defense. To obtain high-quality products at low cost, the composites industry continues seeking for numerical simulation tools to predict the manufacturing processes instead of prototype testing and trials. Regarding the attractive liquid composite molding (LCM) process, it provides the possibility to produce net shape parts from composites. The challenges are how to identify the primary physics of LCM processes and develop mathematical models to represent them. Models need to be both accurate and efficient, which is not easy to achieve.

To model LCM processes, we have one option that describes all physics at the macroscopic scale. The fundamental continuum mechanics principles, e.g., mass balance, momentum balance, energy balance, and entropy inequality, help us developing models. In this regard, the theory of porous media (TPM), which relies on the concept of volume fractions, can explain the problems of the saturated/unsaturated multi-phase materials. Darcy's law describes the relation between the flow velocity and the pressure gradient, without accounting for the dual-scale flow. The air and resin compose the homogenized flow at the infusion stage. The existence of the capillary pressure influences the flow front, which has been revealed in this thesis. The finite element method is employed to solve for the homogenized flow pressure, and the degree of saturation with the staggered approach, especially the Streamline-Upwind/Petrov-Galerkin (SUPG) method is implemented to eradicate the stability problem.

As to the fiber preform response, an assumption of shell kinematics is made to reduce the model from a full 3-D problem to a shell-like problem. Given this, an explicit formulation is obtained to express the normal directional stretch as a function of homogenized flow pressure. This model has been verified and validated by a resin infusion experiment. The model mimics the preform relaxation and lubrication mechanisms successfully and efficiently.

So far, the works mentioned above aimed at the isothermal infusion stage. However, resin flow development, heat transfer, and resin curing are strongly interrelated during the whole LCM process. The holistic simulation of both the infusion stage and the curing stage is carried out in this thesis. Finally, we propose a system of coupled models to help process engineers to design and control process parameters by using virtual numerical experiments instead of the traditional trial-and-error approach.

Keywords: Liquid composite molding; Porous media theory; Process modeling; Resin cure; Fabric composites; Polymer composites

to Wuhan City,
January 23 ∼ April 8, 2020

Preface

The work in this thesis was carried out from September 2015 to May 2020 at the Division of Material and Computational Mechanics, Department of Industrial and Materials Science, Chalmers University of Technology. The research was financially supported by the Swedish Research Council (Vetenskapsrådet) grant no.621-2013-3907. Some of the numerical simulations presented herein were performed on resources at the Chalmers Centre for Computational Science and Engineering (C3SE) provided by the Swedish National Infrastructure for Computing (SNIC).

Acknowledgements

Firstly, I would like to express my sincere gratitude to my supervisor Prof. Ragnar Larsson for the continuous support of my Ph.D. study and the related research.

I thank my colleagues and friends at the division of Material & Computational Mechanics. For the stimulating discussions, for all the fun we have had in the past years, for enlightening me the first glance of research, and for the rewarding workplace.

I also want to thank Prof. Leif Asp and all composite group-mates for constructive suggestions in meetings. Moving on, I want to express my appreciation to Prof. Magnus Ekh, who is the best teacher I have ever met, for sharing his infinite knowledge of mechanics with me.

Last but not least, I want to thank my parents, my dearest wife, and her parents for supporting me spiritually throughout my life.

Göteborg, April 2020

Da Wu

Thesis

This thesis consists of an extended summary and the following appended papers:

Paper A Da Wu, Ragnar Larsson "Homogenized free surface flow in porous media for wet-out processing" *International Journal for Numerical Methods in Engineering* (2018). ISSN: 00295981. DOI: 10.1002/nme.5812

Paper B Da Wu, Ragnar Larsson "A shell model for resin flow and preform deformation in thin-walled composite manufacturing processes" *International Journal of Material Forming* (2019). ISSN: 1960-6214. DOI: 10.1007/s12289-019-01517-z

Paper C Da Wu, Ragnar Larsson, Mohammad S. Rouhi "Modeling and experimental validation of the VARTM process for thin-walled preforms" *Polymers* (2019). ISSN: 2073-4360. DOI: 10.3390/polym11122003

Paper D Da Wu, Ragnar Larsson, Brina Blinzler "A preform deformation and resin flow coupled model including the cure kinetics and chemo-rheology for the VARTM process" *Submitted for publication* (2020).

The appended papers were prepared in collaboration with co-authors. The author of this thesis was responsible for the major progress of the works in the papers, i.e., took part in formulating the theory, led the planning of the papers, developed the numerical implementation, carried out the numerical simulations, designed the experiment, applied for funding, and prepared the manuscript.

OTHER PUBLICATIONS

- ✠ Da Wu, Ragnar Larsson "A model for predicting free surface flow of the RTM process" in *21st International Conference on Composite Materials*, Xi'an China, Aug. 2017.
- ✠ Ragnar Larsson, Da Wu "SUPG stabilized free surface flow at composites processing" in *VII International Conference on Computational Methods for Coupled Problems in Science and Engineering*, Rhodes Island Greece, Jun. 2017.
- ✠ Da Wu, Ragnar Larsson "Planar infusion flow in deformable thin-walled composite components with deformable preform" in *14th International Conference on Flow Processes in Composite Materials*, Luleå Sweden, Jun. 2018.
- ✠ Da Wu, Ragnar Larsson, Mohammad S. Rouhi "Modeling and experimental validation of the VARTM process" in *22nd International Conference on Composite Materials*, Melbourne Australia, Aug. 2019.

Contents

Part I
Extended Summary

1 Introduction

1.1 Background

During the last few decades, the application of the polymer matrix composite (PMC) materials has become broader and broader, from the traditional marine, aerospace, infrastructure, and sport industries to the medicine and battery technologies [1]. The evolution of the PMCs application accompanies the revolution of manufacturing processes. The composites manufacturing aims to combine the best properties of fibers and resins, in the meanwhile, minimize their weaknesses. Åström B.T. [2] and Advani S.G. & Hsiao K.T. [3] wrote books about manufacturing processes, resources for material property data, as well as the process modeling methods. The books give very detailed qualitative insight into the materials and processes addressing the issues encountered from designing to shop floor manufacturing [4]. The characteristics of the processing methods can be classified into three types, 1) short fiber processing, 2) thermoplastic resin processing, and 3) thermoset resin processing.

The *injection molding process* is one of the processes for short fiber reinforced PMCs. This type of process uses the extruder to melt and mix the pellets that contain thermoplastic resin and chopped short fibers, then the suspension is compressed into a rigid mold to form the final shape. Alternately, the *compression molding process* is commonly applied in the automotive industry to produce sheet form components. The stack of precursor materials that are made from thermoset/thermoplastic resins and chopped fibers are placed in the rigid mold, then the upper mold presses the precursor materials and squeezes the resins and fibers filling the mold cavity. Apart from chopped fibers, nanoparticles can be filled with polymers as well, for the purpose of improving the mechanical, thermal, and electrical properties of composites.

Regarding the composites of thermoplastic resin with long fibers, the *sheet forming process* is usually adopted. In this process, a stack of continuous or long fibers reinforced thermoplastic prepregs are heated firstly, then stamped to the shape of the mold cavity. The *thermoplastic filament winding process* aims to produce high-pressure vessels and pipes. In this type of process, the continuous fibers are wetted by the molten thermoplastic resins and wound over the mandrel through a winding head. The *pultrusion process* is one of the options to produce high volume fraction and unidirectional fiber composites. In the process, the impregnated fibers are pulled through a half-heated and half-cooled die. Regarding more complex PMC products, the *continuous compression molding process* can be applied. During this process, series pressing tools are connected and separated to handle different operations sequentially.

Another category of process is the *liquid composite molding* (LCM) *process*, which is usually used to produce advanced composite materials. The idea of this class of process

is to transfer the liquid resin from a reservoir into the fiber preform that is formed from fabrics. The fabrics are among types of random mat, woven, and stitched non-crimp fabrics. The thermoset resin is usually adopted because of its low viscosity (0.05 Pa·s to 0.5 Pa·s). This type of resin can impregnate the voids inside the fiber preform easily. The liquid thermoset resin is cured to solid polymer matrix materials through a series of steps, e.g., chemical reaction, heats evolution, volatiles evolution, increase of viscosity, gelation, and vitrification. The other option is using the thermoplastic resin that usually has very high viscosity (10^2 Pa·s to 10^6 Pa·s). The high viscosity makes the resin very difficult to fill into the fiber preform. Thus, the heating is needed to melt the thermoplastic from the solid phase to the liquid phase.

The *resin transfer molding* (RTM) *process* is a member of the LCM family. In this process, the positive pressure drives the resin into the fiber preform that is enclosed in a mold cavity, until the voids are filled by resins. The RTM process can be applied to produce high performance load-bearing structural parts. Figure 1.1a shows typical RTM process steps. Firstly, the fabric plies are draped on the mold surface. While draping, the fabric plies may be glued with the tackifier to keep bounding during the infusion stage. Secondly, the mold is closed by a rigid cover and clamped. Now the injection starts, the resin is injected into the fiber preform under positive pressure. At the moment, resin flows out the vents, the infusion process is cut off, and let the resin cure. At this stage, the mold could be heated up as resin curing demands. Until the consolidation of resin is finished, the mold is ready to open.

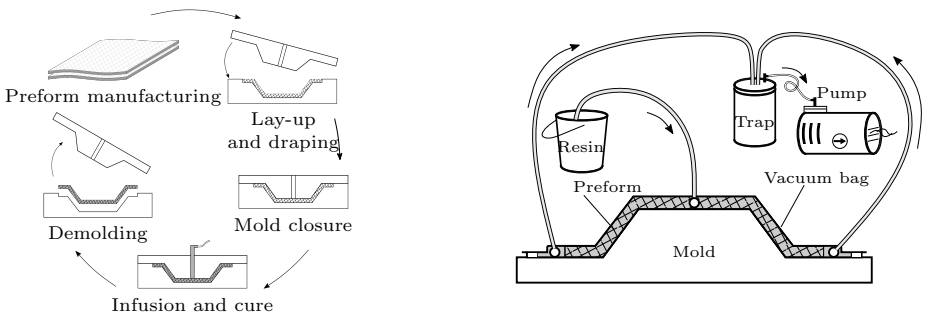

(a) (b)

Figure 1.1: Illustrations of the (a) RTM process steps and (b) VARTM process.

To overcome various issues of the RTM process, the composite material manufacturers developed many variational processes. For large-scale PMCs productions, the vacuum assisted resin transfer molding (VARTM) and the Seemann's composites resin infusion molding process (SCRIMP) inherit from RTM. The modified VARTM, vacuum-induced preform relaxation (VIPR) reduces the fill time. The fast remotely actuated channeling (FASTRAC) can create temporary race-tracking channels to accelerate the process comparing with the RTM process. There are still other modified versions, e.g., light RTM (LRTM), structural reaction injection molding (S-RIM), co-injection resin transfer molding

(CIRTM), compression resin transfer molding (CRTM) and resin infusion between double flexible tooling (RIDFT).

The *vacuum assisted resin transfer molding* (VARTM) *process* belongs to the type of closed-mold method, which can be used to manufacture large-scale PMCs. The process inherits the advantages of RTM, e.g., low volatile organic compounds emission, high quality, and clean operating environment. Also, this process method is flexible and scalable, and usually, the tooling cost is low.

A feature of the VARTM is that the preform is closed by the easily deformed semi-permeable membrane and compressed by the atmospheric pressure. The preform is assembled as a sandwich that consists of fiber networks, peel ply, flow distribution media, and helical tubes. Due to this low-pressure requirement, the VARTM process can be operated like the open mold process, which is suitable for one-piece large-scale structures. A significant difference between the RTM and the VARTM is the injection pressure. In the RTM process, because of the rigid mold cover is strong enough, the injection pressure can be dramatically higher than the environmental pressure, which leads to a positive pressure environment inside the mold cavity. However, this is not feasible in the VARTM process. The injection pressure in the VARTM process is usually equal to 1 atm, so the pressure difference is contributed from the internal mold vacuum. This vacuum environment will compress the preform to the lower mold and drive the resin transferring into the preform.

Figure 1.1b illustrates the VARTM process briefly. Concerning the large or complex shape component and long filling time, the lower mold can be heated for controlling the resin viscosity and managing the curing cycle (as the OOA process desires). What is more, the resin inlets and outlets should be adjusted to generate versatile resin flow paths for better infusion quality and shorter filling time.

1.2 Polymer matrices and fibers

Polymer resin plays the role of the matrix phase of the composite material. The polymers bind the fibers together and provide the tolerance and durability of the composite materials. In addition, the polymer matrix also undertakes the compression and shear loads. In the context of LCM processes, the thermoset materials are usually chosen. The low viscosity (50 to 500 times more viscous than water) makes the thermoset readily flowing into and filling out the voids in the dry fiber preform. A particular step that is named as curing is taken to consolidate the liquid resin to the solid form. In general, polymers are high molecular weight compounds that consist of many repeated small segments. The smallest elements (monomer) are assembled into a polymer through chemical reactions of the poly-condensation and the poly-addition. Thermosets initially consist of molecule chains with weak bonds. Chemical reactions build covalent bonds between polymer chains, which is called cross-linking. The term curing denotes the process of cross-linking. During the curing, more and more polymer chains are bonded together until the entire bulk of polymer has been cross-linked. The strong covalent bonds make the thermoset matrices high thermal and mechanical performances. The viscosity of the thermoset is usually low, between 0.05 Pa·s to 0.5 Pa·s. Thus, thermosets are easy to flow into the voids inside the fiber preform. Because of this characteristic, the thermoset is usually used in LCM

processes.

Another class of polymers is thermoplastic. Thermoplastic polymers can be either amorphous or semicrystalline. The polymer chains of thermoplastics are long and associated with the van der Waals' forces. Due to these characteristics, thermoplastics at the room temperature are solid. During the processing, thermoplastics need to be heated and melted to the liquid phase, whose viscosity is between 10^2 Pa·s and 10^6 Pa·s. The final thermoplastic matrix materials are formed from cooling instead of curing. The rate of cooling (cooling dynamics) highly affects the properties. The advantage of thermoplastic matrices is their recyclable nature and higher toughness than thermosets. However, the high viscosity makes thermoplastics difficult to apply in LCM processes.

Fibers in PMC materials provide stiffness and strength to undergo external loads. Glass, carbon, polymer, and natural materials can be used to make fibers. The advanced composites are made by continuous fibers. A tow of fibers contains 100 to 48000 single fibers laying together as an elliptical cross-section. By weaving, stitching, knitting, or braiding fiber tows together, we can obtain fabric reinforcements, which can be combined to create preforms that are tailored for the particular part geometry and the property requirement. If fiber tows are aligned in one direction to create fabrics, this type of fabric can reach very high fiber volume fraction, in-plane strengths, and stiffness. Another type of fabric is made from interlaced fiber tows, which form 2-D or 3-D interlocked textile structures. In this regard, the composite materials yield high stiffness and strength both in- and out-plane directions, which gives the designer more freedom to fulfill the desired requirements.

In this thesis, we will focus on carbon fiber and thermoset resin. The continuous fibers in sheet fabrics will be used for preforms.

1.3 Aim, scope and limitations

The purpose of this thesis work is to develop a system of mathematical models for simulating the holistic LCM processes, especially for the RTM and VARTM processes. To this end, some research objectives are listed as follows:

- develop a three-phase porous media model for the RTM process;
- develop a shell model for describing the fiber networks swelling and compaction in the VARTM process;
- include the cure kinetics and chemo-rheology in models to simulate the non-isothermal VARTM process;
- carry out experiments for the verification and validation of models.

The work is limited to model the liquid composite molding process at the macroscopic level. The fluid-solid interaction is based on the theory of porous media, plus the limited low flow rate. The microscale fiber structures and the microflow in the vicinity of the fiber bundles are not considered herein. The gravity is neglected in the modeling. In addition, the preform is considered as thin-walled and the through-thickness flow is neglected.

Regarding the non-isothermal process, we assume that the heat transfer between the preform and the resin/air mixed fluid is instantaneous.

2 Manufacturing process modeling

The process modeling can be considered on two different scales. When the modeling is at the macroscale, the interest is in the overall resin flow development and the global deformation of the material. So, the scale is usually the order of millimeters. This physics can be described by the continuum mechanics, or to be more specific, the porous media theory. This approach can exam the overall relations between the processing parameters, e.g., flow rate, pressure, temperature, and fabric structure. However, the phenomena at the microscale (a few microns) will be ignored. In this regard, the multiscale process modeling is also interested.

The RTM and VARTM processes include the low viscosity thermoset resin and woven/stitched fabrics. From the macroscale point of view, the processes can be interpreted as liquid resin infiltrating into the porous fiber network. Thus, the physical process can be modeled as Darcy flow transporting in porous media. Moreover, heat transfer, cure kinetics and chemo-rheology are also crucial facts. In this thesis, we focus on using the porous media theory to model the macroscale physics for RTM and VARTM processes, and including the exothermic curing.

2.1 The porous media theory

The porous medium is a kind of material that consists of solid constituents and closed or open pores. The pores can be flooded with fluids or gas and interact with the neighboring solid. Reinhard Woltman [5] built a systematical soil mechanics and porous bodies framework and introduced the essential concept – volume fraction. These works are known as the prerequisites for developing the porous media theory. After Woltman's concept of volume fraction, around the mid-19th, the mixture theory and the porous bodies theory were developed significantly. Delesse's concept of surface fractions [6] became the most fundamental contribution to the porous media theory. Then the first phenomenological mixture theory was done by Fick [7]. Fick's contribution was Fick's first and second diffusion laws.

Josef Stefan [8] for the first time derived the motion and mass balance equations for a mixture of two gases following the continuum mechanics framework and the concept of volume fraction with the consideration of the porosity of the porous solid. This work gives the foundation of the mixture theory, and it becomes the symbol of the classical era of the development of the porous media theory.

Due to it is almost impossible to indicate the exact location of solid and pores, we must describe it alternately, viz. *volume fraction concept*. By doing so, the discontinuous porous media is interpreted as a smeared model. The motion, deformation, stress, pressure, and other state variables are averaged statistically from the intrinsic values in the control volume. Thus, the (partial-)saturated porous media can be considered as the mixture of all constituents at a certain material position $\boldsymbol{X}^{\alpha}$ (or $\boldsymbol{x}$). With this substitute model, the continuum mechanics methods can be applied to handle the porous media problem.

Once the volume fraction concept is employed, the micromechanical effects are also "smeared" into the model. Following the porous media theory, the microscale quantities are

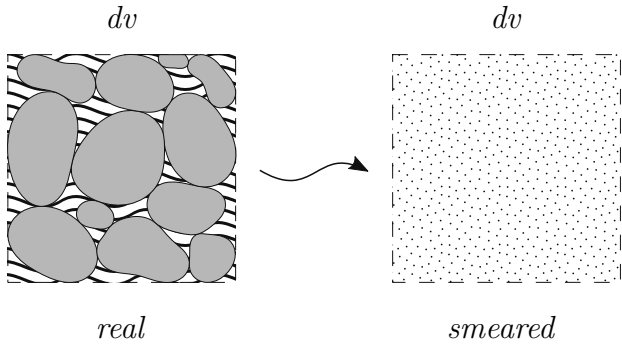

Figure 2.1: The real porous media composed of solid and liquid phases are averaged statistically to a smeared body.

represented by the macro-mechanical quantities instead. However, an inevitable problem is still rising: only $\alpha - 1$ equations will be derived in the α constituents porous media, i.e., the problem cannot be closed. In order to work this problem out, the microscale understanding must be included.

2.1.1 The volume fraction concept

To explain the volume fraction concept, we introduce some notations. Assuming a porous medium consists of the solid phase controlling the domain B_s that bounded by ∂B_s. The v^α represents the real volumes of the constituent α among κ different constituents. In Figure 2.2, the average volume element locates at $\boldsymbol{x}$, $\boldsymbol{r}$ points the position of the α constituent that has volume dv_μ. Let's define an indicator function as

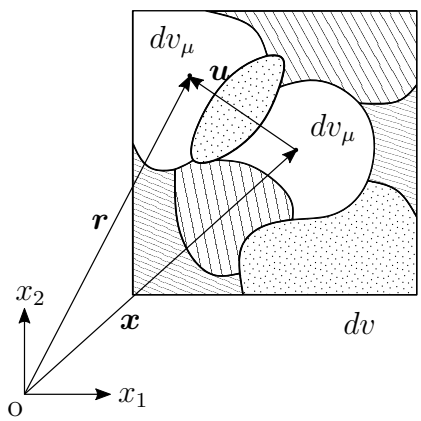

Figure 2.2: The average volume element of the multiple constituents porous media.

$$\chi^{\alpha} = \chi^{\alpha}(\boldsymbol{r}, t) = \begin{cases} 1 & if\ \boldsymbol{r} \in\ dv^{\alpha}, \\ 0 & if\ \boldsymbol{r} \in\ dv^{\beta}, \end{cases}\ \alpha \neq \beta\ . \tag{2.1}$$

So the volume element of the constituent α in the total volume element can be expressed by

$$dv^{\alpha}(\boldsymbol{x}, t) = \sum_{i}^{\kappa} dv_{\mu}^{i} = \int_{dv} \chi^{\alpha}(\boldsymbol{r}, t)\, dv_{\mu}\ . \tag{2.2}$$

Now we can formulate the volume fraction as

$$n^{\alpha}(\boldsymbol{x}, t) = \frac{1}{dv} \int_{dv} \chi^{\alpha}(r, t)\, dv_{\mu} = \frac{dv^{\alpha}}{dv}\ , \tag{2.3}$$

with the constraint,

$$\sum_{i=1}^{\kappa} n^{i} = 1. \tag{2.4}$$

If the real or intrinsic density of α constituent at location r can be defined as $\rho^{\alpha \boldsymbol{r}} = \rho^{\alpha \boldsymbol{r}}(\boldsymbol{r}, t)$, thus the real density at the $\boldsymbol{x}$ yields $\rho^{\alpha} = \rho^{\alpha}(\boldsymbol{x}, t)$, and of cause the macroscale quantity is $\rho^{\alpha \boldsymbol{x}} = \rho^{\alpha \boldsymbol{x}}(\boldsymbol{x}, t)$. Now we can obtain two critical relations of the density from the volume fraction concept

$$\begin{aligned} \rho^{\alpha}(\boldsymbol{x}, t) &= \frac{1}{dv^{\alpha}} \int_{dv} \rho^{\alpha \boldsymbol{r}}(\boldsymbol{r}, t)\, \chi^{\alpha}(\boldsymbol{r}, t)\, dv_{\mu} \\ &= \rho^{\alpha \boldsymbol{r}}(\boldsymbol{r}, t)\, \frac{dv^{\alpha}}{dv^{\alpha}} \\ &= \rho^{\alpha \boldsymbol{r}}\ , \end{aligned} \tag{2.5}$$

and

$$\begin{aligned} \rho^{\alpha \boldsymbol{x}}(\boldsymbol{x}, t) &= \frac{1}{dv} \int_{dv} \rho^{\alpha \boldsymbol{r}}(\boldsymbol{r}, t)\, \chi^{\alpha}(\boldsymbol{r}, t)\, dv_{\mu} \\ &= \rho^{\alpha \boldsymbol{r}}(\boldsymbol{r}, t)\, \frac{dv^{\alpha}}{dv} \\ &= n^{\alpha}(\boldsymbol{x}, t) \rho^{\alpha \boldsymbol{r}}\ . \end{aligned} \tag{2.6}$$

For the liquid-air mixed porous media, the homogenized fluid density can be obtained

following the above approach as

$$\begin{aligned}
\rho^{f\boldsymbol{x}}(\boldsymbol{x},t) &= \frac{1}{dv}\int\limits_{dv}\rho^{l\boldsymbol{r}}(\boldsymbol{r},t)\,\chi^{l}(\boldsymbol{r},t)\,dv_{\mu} + \frac{1}{dv}\int\limits_{dv}\rho^{g\boldsymbol{r}}(\boldsymbol{r},t)\,\chi^{g}(\boldsymbol{r},t)\,dv_{\mu} \\
&= \rho^{l\boldsymbol{r}}(\boldsymbol{r},t)\,\frac{dv^{l}}{dv} + \rho^{g\boldsymbol{r}}(\boldsymbol{r},t)\,\frac{dv^{g}}{dv} \\
&= n^{l}\rho^{l\boldsymbol{r}} + n^{g}\rho^{g\boldsymbol{r}} \\
&= n^{f}\left(\xi\rho^{l\boldsymbol{r}} + (1-\xi)\rho^{g\boldsymbol{r}}\right) \\
&= n^{f}\rho^{f\boldsymbol{r}} \\
&= n^{f}\rho^{f}\ ,
\end{aligned} \tag{2.7}$$

where $\rho^{f\boldsymbol{r}}$ is the homogenized intrinsic density of the mixture of liquid and gas. The degree of saturation ξ is defined as

$$\xi = \frac{n^{l}}{n^{f}} \text{ and } 0 \leqslant \xi \leqslant 1\ , \tag{2.8}$$

where $n^{f} = n^{l} + n^{g}$. Thus, from Equation (2.7), we can obtain the expression of the homogenized fluid density as

$$\begin{aligned}
\rho^{f\boldsymbol{r}} &= \xi\rho^{l\boldsymbol{r}} + (1-\xi)\rho^{g\boldsymbol{r}} \rightsquigarrow \\
\rho^{f} &= \xi\rho^{l} + (1-\xi)\rho^{g}\ .
\end{aligned} \tag{2.9}$$

By applying the same homogenization approach, we can obtain the mixture pressure as

$$p^{f} = \xi p^{l} + (1-\xi)p^{g}\ . \tag{2.10}$$

Regarding the existence of capillary pressure, Gray and Hassanizadeh [9] derived the expression, $p^{c}(\xi) = p^{g} - p^{l}$, in 1991. By using this expression, we can build a connection between the liquid and gas pressures as

$$\begin{aligned}
p^{l} &= p^{f} - (1-\xi)p^{c}, \text{ and} \\
p^{g} &= p^{f} + \xi p^{c}\ .
\end{aligned} \tag{2.11}$$

Moreover, the gas pressure p^{g} can be obtained from the universal gas law as

$$p^{g} = \frac{\rho^{g}}{k^{g}} = \frac{R\Theta\rho^{g}}{m^{g}}\ , \tag{2.12}$$

where m^{g} is the gas molar mass, R denotes the ideal gas constant and Θ is the absolute temperature of the gas.

2.1.2 Kinematics

In order to address the kinematics, we need to make two certain assumptions:

- At a certain time t, all of the constituents share the same spatial point $\boldsymbol{x}$, but the trajectories are from different reference configurations at $t = t_0$;
- thus, every constituent in the heterogeneous mixture has an independent motion.

Based on these assumptions, we define the deformation mapping following the continuum mechanics framework,

$$\boldsymbol{x} = \boldsymbol{\varphi}^s\left(\boldsymbol{X}^s\right) = \boldsymbol{\varphi}^f\left(\boldsymbol{X}^f\right) \ , \ \boldsymbol{X}^s \neq \boldsymbol{X}^f \ , \ \boldsymbol{\varphi}^s \neq \boldsymbol{\varphi}^f \ , \tag{2.13}$$

where $\boldsymbol{\varphi}^s$ and $\boldsymbol{\varphi}^f$ represent the deformation mapping of the solid and fluid phases respectively. Thus the corresponding deformation gradient can be defined as

$$\boldsymbol{F}^\alpha = \boldsymbol{\varphi}^\alpha \otimes \boldsymbol{\nabla}_{\boldsymbol{X}} \ . \tag{2.14}$$

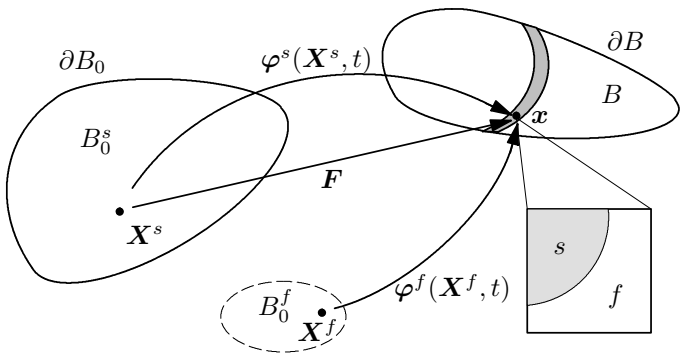

Figure 2.3: The motion of the solid and fluid phases for a saturated porous media.

Moreover, the Jacobian J^α can be obtained as

$$J^\alpha = \det\left(\boldsymbol{F}^\alpha\right) > 0 \ . \tag{2.15}$$

Next, the velocity of each constituent can be defined as

$$\boldsymbol{v}^\alpha = \left(\dot{\boldsymbol{x}}\right)_\alpha = \left(\dot{\boldsymbol{\varphi}^\alpha}\right)_\alpha = \frac{D^\alpha \boldsymbol{\varphi}^\alpha\left(\boldsymbol{X}^\alpha\right)}{Dt} \ , \tag{2.16}$$

where the operator $\left(\dot{\bullet}\right)_\alpha$ denotes the material time derivative for the constituent α.

From the definition, we know the intrinsic velocity of the constituent α. In order to include the velocity in the constitutive relation – Darcy's law, we need a relation between the intrinsic velocity $\boldsymbol{v}^f$and Darcy's velocity $\boldsymbol{v}^{df}$. Let f_w represent the area of a cross-section of a cylinder where the fluid can pass through. Thus we obtain $Q = f_w \boldsymbol{v}^f$, where f_w also denotes the porosity on the cross-section. From Deless [6], we notice that the surface porosity is equal to the volume porosity, i.e., $f_w = n^f$. Finally, we conclude,

$$Q = n^f \boldsymbol{v}^f = \boldsymbol{v}^{df}. \tag{2.17}$$

When the cylinder is deforming with the velocity of $\boldsymbol{v}^s$, Equation (2.17) turns to

$$\boldsymbol{v}^{df} = n^f \boldsymbol{v}^{rf}, \tag{2.18}$$

where $\boldsymbol{v}^{rf} = \boldsymbol{v}^f - \boldsymbol{v}^s$ is the relative velocity, or the seepage velocity.

2.1.3 Mass balance

In this section, we consider the mass balance for the individual constituent α. The mass balance can be expressed by words as – the rate of change of the mass M^α is equal to the mass supply $\int\limits_{B_\alpha} \bar{\rho}^{\alpha\boldsymbol{x}} dv = \int\limits_{B_\alpha} n^\alpha \bar{\rho}^\alpha dv$, where $\bar{\rho}^\alpha$ denotes the density supply. The formulation reflects,

$$(\dot{M}^\alpha)_\alpha = \overline{\left(\int\limits_{B_\alpha} \rho^{\alpha\boldsymbol{x}} dv \right)}^{\cdot}_{\alpha} = \int\limits_{B_\alpha} \bar{\rho}^{\alpha\boldsymbol{x}} dv \tag{2.19}$$

From the fundamental continuum mechanics knowledge, we conclude the mass balance equation for single phase α

$$\frac{\partial \rho^{\alpha\boldsymbol{x}}}{\partial t} + \boldsymbol{\nabla} \cdot (\rho^{\alpha\boldsymbol{x}} \boldsymbol{v}^\alpha) = \bar{\rho}^{\alpha\boldsymbol{x}}. \tag{2.20}$$

If using a homogenized velocity $\boldsymbol{v}$ substitute the intrinsic velocity $\boldsymbol{v}^\alpha$ of each constituent, we obtain a mass balance equation for the bulk heterogenous mixture

$$\sum_{\alpha=1}^{\kappa} \left[\frac{\partial n^\alpha \rho^\alpha}{\partial t} + \boldsymbol{\nabla} \cdot (n^\alpha \rho^\alpha \boldsymbol{v}) \right] = \sum_{\alpha=1}^{\kappa} n^\alpha \bar{\rho}^\alpha \ . \tag{2.21}$$

As it is mentioned previously, the problem is not closed. For a two-phase porous media problem, we introduce an auxiliary equation from the constraint (2.4) to close the problem

$$(\dot{n^s})_s + (\dot{n^f})_s = 0 \ , \tag{2.22}$$

and

$$(\dot{n^s})_s + (\dot{n^f})_f - \boldsymbol{\nabla} \cdot \left(n^f \boldsymbol{v}^{rf} \right) = 0 \ , \tag{2.23}$$

From Equations (2.22) and (2.23), we yield

$$(\dot{n^f})_f = (\dot{n^f})_s + \boldsymbol{\nabla} \cdot \left(n^f \boldsymbol{v}^{rf} \right) \ , \tag{2.24}$$

where n^f can be replaced by other variables.

Until now, we have a closed mass balance equation system for the two-phase (solid and fluid) porous media problem. In this thesis, the fluid phase consists of gas and liquid. Thus, the α will be replaced by solid s, resin l, gas g, and the homogenized fluid f. If the mass supply is ignored, Equation (2.19) can be extended to

$$\begin{aligned} (\dot{M^s})_s = 0 \rightsquigarrow \\ \dot{\overline{n^s \rho^s}} + n^s \rho^s \boldsymbol{\nabla} \cdot \boldsymbol{v}^s = 0 \ , \end{aligned} \tag{2.25}$$

$$
\begin{aligned}
\left(\dot{M^f}\right)_f = 0 \rightsquigarrow \\
\left(\dot{M^f}\right)_s + \boldsymbol{\nabla}\cdot\left(n^f\rho^f\boldsymbol{v}^{rf}\right) = 0 \rightsquigarrow \\
\dot{\overline{n^f\rho^f}} + n^f\rho^f\boldsymbol{\nabla}\cdot\boldsymbol{v}^s + \boldsymbol{\nabla}\cdot\left(n^f\rho^f\boldsymbol{v}^{rf}\right) = 0\ ,
\end{aligned}
\tag{2.26}
$$

By summarizing Equations (2.25) and (2.26) together, we can obtain

$$
\dot{n}^s + \dot{n}^f + n^s\boldsymbol{\nabla}\cdot\boldsymbol{v}^s + (1-n^s)\boldsymbol{\nabla}\cdot\boldsymbol{v}^s + n^s\frac{\dot{\rho}^s}{\rho^s} + n^f\frac{\dot{\rho}^f}{\rho^f} + \frac{1}{\rho^f}\boldsymbol{\nabla}\cdot\left(\rho^f n^f\boldsymbol{v}^f\right) = 0\ . \tag{2.27}
$$

From Equations (2.17) and (2.22), we can simplify Equation (2.27) to

$$
\boxed{\boldsymbol{\nabla}\cdot\boldsymbol{v}^s + n^s\frac{\dot{\rho}^s}{\rho^s} + n^f\frac{\dot{\rho}^f}{\rho^f} + \frac{1}{\rho^f}\boldsymbol{\nabla}\cdot\left(\rho^f\boldsymbol{v}^{df}\right) = 0}\ . \tag{2.28}
$$

Similarly, when only the resin constituent is considered, Equation (2.19) can be extended to

$$
\begin{aligned}
\left(\dot{M^l}\right)_l = 0 \rightsquigarrow \\
\left(\dot{M^l}\right)_s + \boldsymbol{\nabla}\cdot\left(n^l\rho^l\boldsymbol{v}^{rl}\right) = 0 \rightsquigarrow \\
\dot{\overline{n^l\rho^l}} + n^l\rho^l\boldsymbol{\nabla}\cdot\boldsymbol{v}^s + \boldsymbol{\nabla}\cdot\left(n^l\rho^l\boldsymbol{v}^{rl}\right) = 0 \rightsquigarrow \\
\dot{n^l} + n^l\frac{\dot{\rho^l}}{\rho^l} + n^l\boldsymbol{\nabla}\cdot\boldsymbol{v}^s + \boldsymbol{\nabla}\cdot\boldsymbol{v}^{dl} = 0 \rightsquigarrow \\
\dot{n^f}\xi + \dot{\xi}n^f + n^l\frac{\dot{\rho^l}}{\rho^l} + n^f\xi\boldsymbol{\nabla}\cdot\boldsymbol{v}^s + \boldsymbol{\nabla}\cdot\boldsymbol{v}^{dl} = 0\ .
\end{aligned}
\tag{2.29}
$$

By inserting $\dot{\rho}^l = 0$ (assuming the resin is incompressible) and $\dot{n}^f = n^s\boldsymbol{\nabla}\cdot\boldsymbol{v}^s$ into Equation (2.29), we can obtain

$$
\boxed{\dot{\xi}n^f + \xi\boldsymbol{\nabla}\cdot\boldsymbol{v}^s + \boldsymbol{\nabla}\cdot\boldsymbol{v}^{dl} = 0}\ . \tag{2.30}
$$

So far we have derived two governing Equations (2.28) and (2.30), which are named as *pressure equation* and *saturation equation*, respectively. In Equations (2.28) and (2.30), the term $\boldsymbol{\nabla}\cdot\boldsymbol{v}^s$ can be replaced by

$$
\boldsymbol{\nabla}\cdot\boldsymbol{v}^s = \frac{\dot{J}^s}{J^s} = \frac{\dot{J}}{J}\ . \tag{2.31}
$$

2.1.4 Balance of momentum

The balance of momentum tells that the rate of change of the linear momentum is equal to the sum of resultant forces. If the density supply is ignored, the formulation shows

$$
\dot{\overline{\left(\int_{B_\alpha}\rho^{\alpha\boldsymbol{x}}\boldsymbol{v}^\alpha dv\right)}}_\alpha = \int_{B_\alpha}\left(\rho^{\alpha\boldsymbol{x}}\boldsymbol{b}^\alpha + \hat{\boldsymbol{p}}^\alpha\right)dv + \int_{\partial B_\alpha}\boldsymbol{t}^\alpha ds\ , \tag{2.32}
$$

where $\rho^{\alpha\boldsymbol{x}}\boldsymbol{b}^{\alpha}$ is the body force, $\hat{\boldsymbol{p}}^{\alpha}$ is the interaction force, and $\boldsymbol{t}^{\alpha}$ is the surface traction. Given Cauchy's principle and the divergence theorem, the balance of momentum for the α phase is formulated as

$$\boldsymbol{\sigma}^{\alpha}\cdot\boldsymbol{\nabla}+\rho^{\alpha\boldsymbol{x}}\boldsymbol{b}^{\alpha}+\hat{\boldsymbol{p}}^{\alpha}=\rho^{\alpha\boldsymbol{x}}(\dot{\boldsymbol{v}^{\alpha}})_{\alpha}\ . \tag{2.33}$$

If the common velocity $\boldsymbol{v}$ and acceleration $\boldsymbol{b}$ are introduced, the momentum balance for the whole mixture bulk body can be expressed as

$$\sum_{\alpha=1}^{\kappa}(\boldsymbol{\sigma}^{\alpha}\cdot\boldsymbol{\nabla}+\rho^{\alpha\boldsymbol{x}}\boldsymbol{b}+\hat{\boldsymbol{p}}^{\alpha})=\sum_{\alpha=1}^{\kappa}\rho^{\alpha\boldsymbol{x}}\dot{\boldsymbol{v}}\ . \tag{2.34}$$

In a liquid and gas mixed three-phase porous media problem, we can obtain the linear momentum balance of the whole porous media as

$$\overline{\boldsymbol{\sigma}}\cdot\boldsymbol{\nabla}+\left(\hat{\rho}^{s}+\hat{\rho}^{f}\right)\boldsymbol{b}=\hat{\rho}^{s}\dot{\boldsymbol{v}}^{s}+\hat{\rho}^{f}\left(\dot{\boldsymbol{v}}^{f}+\boldsymbol{v}^{f}\otimes\boldsymbol{\nabla}\cdot\boldsymbol{v}^{rf}\right)\ , \tag{2.35}$$

where $\hat{\rho}^{s}=\rho^{s\boldsymbol{x}}=n^{s}\rho^{s}$, $\hat{\rho}^{f}=\rho^{f\boldsymbol{x}}=n^{f}\rho^{f}$, and $\overline{\boldsymbol{\sigma}}=\boldsymbol{\sigma}^{s}+\boldsymbol{\sigma}^{f}$ is the total stress.

Similarly, we can obtain the linear momentum balance of the solid phase and fluid phase, respectively,

$$\boldsymbol{\sigma}^{s}\cdot\boldsymbol{\nabla}+\hat{\rho}^{s}\boldsymbol{b}+\hat{\boldsymbol{p}}^{s}=\hat{\rho}^{s}\dot{\boldsymbol{v}}^{s}\ , \tag{2.36}$$

$$\boldsymbol{\sigma}^{f}\cdot\boldsymbol{\nabla}+\hat{\rho}^{f}\boldsymbol{b}+\hat{\boldsymbol{p}}^{f}=\hat{\rho}^{f}\left(\dot{\boldsymbol{v}}^{f}+\boldsymbol{l}^{f}\cdot\boldsymbol{v}^{rf}\right)\ , \tag{2.37}$$

where $\hat{\boldsymbol{p}}^{f}=-\hat{\boldsymbol{p}}^{s}$. The term $\boldsymbol{v}^{f}\otimes\boldsymbol{\nabla}=\boldsymbol{l}^{f}$ is the spatial velocity gradient.

2.1.5 Energy balance

The first law of thermodynamics justifies the energy balance, which tells that the rate of change of internal and kinetic energies is balanced by the mechanical power and the thermal power. For an individual constituent α in the porous media, let E, K, W and Q represent internal energy, kinetic energy, mechanical power and thermal power respectively, the balance of energy can be formulated as

$$(\dot{E^{\alpha}})_{\alpha}+(\dot{K^{\alpha}})_{\alpha}=W^{\alpha}+Q^{\alpha}\ . \tag{2.38}$$

After some derivations and using mass and linear momentum balances, the energy balance can be reformulated as

$$\rho^{\alpha\boldsymbol{x}}(\dot{e^{\alpha}})_{\alpha}=\boldsymbol{\sigma}^{\alpha}\colon\boldsymbol{D}^{\alpha}+\rho^{\alpha\boldsymbol{x}}r^{\alpha}-\boldsymbol{\nabla}\cdot\boldsymbol{q}^{\alpha}\ , \tag{2.39}$$

where e^{α} is the specific internal energy, $\boldsymbol{D}^{\alpha}$ is the rate-of-deformation tensor, r^{α} is the energy source, and $\boldsymbol{q}^{\alpha}$ is the heat flux. As previous approaches, let $r^{\alpha}=r$ and $\boldsymbol{q}^{\alpha}=\boldsymbol{q}$ the energy balance for the mixture porous body yields

$$\sum_{\alpha=1}^{\kappa}\rho^{\alpha\boldsymbol{x}}(\dot{e^{\alpha}})_{\alpha}=\sum_{\alpha=1}^{\kappa}(\boldsymbol{\sigma}^{\alpha}\colon\boldsymbol{D}^{\alpha}+\rho^{\alpha\boldsymbol{x}}r-\boldsymbol{\nabla}\cdot\boldsymbol{q})\ . \tag{2.40}$$

More specifically, for the whole porous body without energy source, we have

$$\dot{\hat{e}}+\boldsymbol{\nabla}\cdot\boldsymbol{q}=\overline{\boldsymbol{\sigma}}\colon\boldsymbol{l}^{s}+\boldsymbol{\nabla}\cdot\left(\boldsymbol{\sigma}^{f}\cdot\boldsymbol{v}^{rf}\right)-n^{f}\rho^{f}\boldsymbol{v}^{rf}\cdot\left(\dot{\boldsymbol{v}}^{f}+\boldsymbol{l}^{f}\cdot\boldsymbol{v}^{rf}+\boldsymbol{\nabla}e^{f}\right)\ , \tag{2.41}$$

where $\dot{\hat{e}}=n^{s}\rho^{s}\dot{e}^{s}+n^{f}\rho^{f}\dot{e}^{f}$.

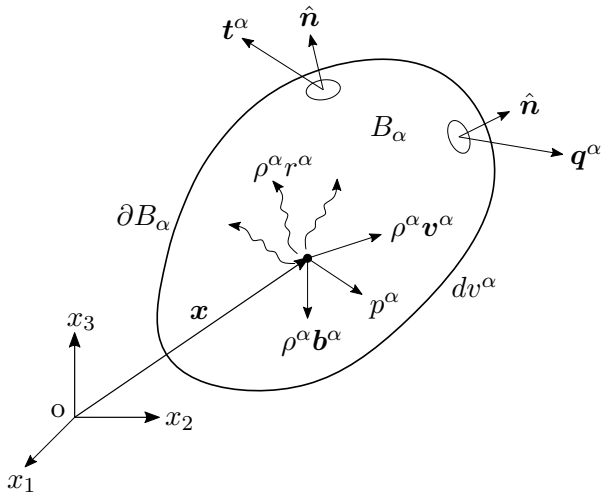

Figure 2.4: Continuum in motion for α phase.

2.1.6 Entropy inequality

The second law of thermodynamics is also known as entropy principle has been used to retrieve constitutive relations since 1963 [10]. Within the mixture body, the summation of the entropy of each constituent should hold the principle. If the supply density is ignored, the entropy inequality (Clausius Duhems inequality) is expressed as

$$\sum_{\alpha=1}^{\kappa} \left(\dot{\mathcal{H}^\alpha}\right)_\alpha \geqslant \sum_{\alpha=1}^{\kappa} Q_\Theta^\alpha \ , \tag{2.42}$$

where $\mathcal{H}^\alpha$ is the entropy of the α constituents, Q_Θ is the summation of supplied entropy and entropy flux, which are defined as

$$\mathcal{H}^\alpha = \int_{B_\alpha} \rho^{\alpha \boldsymbol{x}} s^\alpha \mathrm{d}v \ , \text{ and} \tag{2.43}$$

$$Q_\Theta^\alpha = \int_{B_\alpha} \frac{1}{\Theta} \rho^{\alpha \boldsymbol{x}} r \mathrm{d}v - \int_{\partial B_\alpha} \frac{\boldsymbol{n} \cdot \boldsymbol{q}}{\Theta} \mathrm{d}\Gamma \ , \tag{2.44}$$

where s^α is the specific entropy, and Θ is the absolute temperature.

The local form of the entropy inequality is expressed,

$$\sum_{\alpha=1}^{\kappa} \left[\rho^{\alpha \boldsymbol{x}} \left(\dot{s^\alpha}\right)_\alpha - \frac{1}{\Theta} \rho^{\alpha \boldsymbol{x}} r + \boldsymbol{\nabla} \cdot \left(\frac{\boldsymbol{q}}{\Theta} \right) \right] \geqslant 0 \ . \tag{2.45}$$

In addition, the free Helmholtz energy is formulated as $\psi^\alpha = e^\alpha - \Theta s^\alpha$. For the isothermal condition with the ignorance of energy source, we yield

$$\dot{\hat{e}} + \boldsymbol{\nabla} \cdot \boldsymbol{q} - \dot{\hat{\psi}} + \rho^f n^f \boldsymbol{v}^{rf} \cdot \boldsymbol{\nabla} \left(s^f \Theta \right) - \boldsymbol{q} \cdot \boldsymbol{\nabla} \Theta \geqslant 0 \ , \tag{2.46}$$

where $\dot{\hat{\psi}} = n^s \rho^s \dot{\psi}^s + n^f \rho^f \dot{\psi}^f$. Using Equation (2.41), we obtain

$$\begin{aligned} \left(\boldsymbol{\sigma} - n^f \boldsymbol{\tau}^f\right) : \boldsymbol{l}^s - p^f n^s \frac{\dot{\rho}^s}{\rho^s} - n^s \rho^s \dot{\psi}^s \\ + \left(n^f \boldsymbol{\tau}^f\right) : \boldsymbol{l}^f \\ - p^f n^f \frac{\dot{\rho}^f}{\rho^f} - n^f \rho^f \dot{\psi}^f \\ + \rho^f n^f \boldsymbol{v}^{rf} \cdot \boldsymbol{h}^f \\ - \boldsymbol{q} \cdot \boldsymbol{\nabla}\Theta \geqslant 0 \ , \end{aligned} \tag{2.47}$$

where $\boldsymbol{\sigma}$ is the effective stress that is obtained from Terzaghi effective stress principle

$$\boldsymbol{\sigma} = \overline{\boldsymbol{\sigma}} + p^f \mathbf{1} \ , \text{ and} \tag{2.48}$$

$\boldsymbol{h}^f$ is defined as

$$\boldsymbol{h}^f = -\boldsymbol{\nabla}\psi^f - \left(\dot{\psi^f}\right)_f - \boldsymbol{\nabla}\left(\frac{p^f}{\rho^f}\right) + \frac{\boldsymbol{\nabla}\cdot\left(n^f s^f\right)}{\rho^f} \ , \tag{2.49}$$

Regarding thermoset resin, the viscous part of fluid stress $\boldsymbol{\tau}^f$ is relative small compared with the effective stress $\boldsymbol{\sigma}$. Thus, the entropy inequality for the whole porous body can be simplified as

$$\begin{aligned} \boldsymbol{\sigma} : \boldsymbol{l}^s - p^f n^s \frac{\dot{\rho}^s}{\rho^s} - n^s \rho^s \dot{\psi}^s \\ + \left(n^f \boldsymbol{\tau}^f\right) : \boldsymbol{l}^f \\ - p^f n^f \frac{\dot{\rho}^f}{\rho^f} - n^f \rho^f \dot{\psi}^f \\ + \rho^f n^f \boldsymbol{v}^{rf} \cdot \boldsymbol{h}^f \\ - \boldsymbol{q} \cdot \boldsymbol{\nabla}\Theta \geqslant 0 \ . \end{aligned} \tag{2.50}$$

To guarantee the inequality, we can divide Equation (2.50) to different parts. First, the dissipation produced by the solid phase can be expressed as

$$\mathcal{D}^s = \boldsymbol{\sigma} : \boldsymbol{l}^s - p^f n^s \frac{\dot{\rho}^s}{\rho^s} - n^s \rho^s \dot{\psi}^s \geqslant 0 \ . \tag{2.51}$$

Then, the dissipation related to the viscous part of fluid stress

$$\mathcal{D}^v = \left(n^f \boldsymbol{\tau}^f\right) : \boldsymbol{l}^f \geqslant 0 \ . \tag{2.52}$$

Next, the dissipation related to the fluid $\mathcal{D}^f$

$$\mathcal{D}^f = -n^f p^f \frac{\dot{\rho}^f}{\rho^f} - n^f \rho^f \dot{\psi}^f \geqslant 0 \ . \tag{2.53}$$

The fourth dissipation $\mathcal{D}^i$ reflects the movement of the mixed fluid as

$$\mathcal{D}^i = \rho^f n^f \boldsymbol{v}^{rf} \cdot \boldsymbol{h}^f = \rho^f \boldsymbol{v}^{df} \cdot \boldsymbol{h}^f \geqslant 0 \ . \tag{2.54}$$

The last part is the thermal dissipation

$$\mathcal{D}^\Theta = -\boldsymbol{q} \cdot \boldsymbol{\nabla}\Theta \geqslant 0 \ . \tag{2.55}$$

$\mathcal{D}^\Theta$ is obvious always larger than or equal to zero. In this thesis, we will mainly focus on the fluid phase. Thus, let us consider the dissipation $\mathcal{D}^v$, $\mathcal{D}^f$ and $\mathcal{D}^i$ to check if the inequalities are satisfied. Regarding $\mathcal{D}^i$, let's define $\boldsymbol{v}^{df} = \boldsymbol{K} \cdot \boldsymbol{h}^f$, where $\boldsymbol{K}$ is the positive definite permeability tensor. Thus, we can guarantee $\mathcal{D}^i \geqslant 0$ as

$$\mathcal{D}^i = \rho^f \boldsymbol{v}^{df} \cdot \boldsymbol{h}^f = \rho^f \left(\boldsymbol{h}^f\right)^{\mathrm{T}} \cdot \boldsymbol{K} \cdot \boldsymbol{h}^f \geqslant 0 \ . \tag{2.56}$$

Regarding $\mathcal{D}^f$, we can define ψ^f as a function of mixed fluid pressure p^f and the degree of saturation ξ, i.e., $\psi^f = \psi^f[p^f, \xi]$. Using the results from Equations (2.11) and (2.12), we can obtain

$$\begin{aligned} \mathcal{D}^f = \underbrace{\left(p^f \left(\rho^l - \rho^g + \frac{1-\xi}{k^g} p^c + \frac{1-\xi}{k^g} \xi \frac{\mathrm{d}p^c}{\mathrm{d}\xi}\right) - \left(\rho^f\right)^2 \frac{\partial \psi^f}{\partial \xi}\right)}_{\mathcal{D}^f_A} \dot{\xi} \\ + \underbrace{\left(p^f \frac{1-\xi}{k^g} - \left(\rho^f\right)^2 \frac{\partial \psi^f}{\partial p^f}\right)}_{\mathcal{D}^f_B} \dot{p}^f \ . \end{aligned} \tag{2.57}$$

To make sure $\mathcal{D}^f \geqslant 0$, we need to prove $\mathcal{D}^f_A = 0$ and $\mathcal{D}^f_B = 0$. Before proving these two condition, let us first look at Equation (2.53),

$$\begin{aligned} -n^f p^f \frac{\dot{\rho}^f}{\rho^f} - n^f \rho^f \dot{\psi}^f = \left(-\frac{p^f}{{\rho^f}^2} + \frac{\partial \psi^f}{\partial \rho^f}\right) \dot{\rho}^f \geqslant 0 \rightsquigarrow \\ \frac{\partial \psi^f}{\partial \rho^f} = \frac{p^f}{\left(\rho^f\right)^2} \ . \end{aligned} \tag{2.58}$$

Now, let us rewrite $\mathcal{D}_A^f$,

$$\begin{aligned}
\frac{\left(\rho^f\right)^2}{p^f}\frac{\partial \psi^f}{\partial \xi} &= \\
\frac{\left(\rho^f\right)^2}{p^f}\frac{\partial \psi^f}{\partial \rho^f}\frac{\partial \rho^f}{\partial \xi} &= \\
\frac{\left(\rho^f\right)^2}{p^f}\frac{p^f}{\left(\rho^f\right)^2}\frac{\partial \rho^f}{\partial \xi} &= \\
\frac{\partial \rho^f}{\partial \xi} &= \\
\frac{\partial}{\partial \xi}\left(\xi\rho^l + (1-\xi)\,\rho^g\right) &= \\
\rho^l - \rho^g + \frac{1-\xi}{k^g}p^c + \frac{1-\xi}{k^g}\xi\frac{\mathrm{d}p^c}{\mathrm{d}\xi} &\rightsquigarrow \\
\mathcal{D}_A^f = 0 \quad \square\,. &
\end{aligned} \tag{2.59}$$

Similarly, we can prove

$$\begin{aligned}
\frac{\left(\rho^f\right)^2}{p^f}\frac{\partial \psi^f}{\partial p^f} &= \\
\frac{\left(\rho^f\right)^2}{p^f}\frac{\partial \psi^f}{\partial \rho^f}\frac{\partial \rho^f}{\partial p^f} &= \\
\frac{\left(\rho^f\right)^2}{p^f}\frac{p^f}{\left(\rho^f\right)^2}\frac{\partial \rho^f}{\partial p^f} &= \\
\frac{\partial \rho^f}{\partial \xi} &= \\
\frac{\partial}{\partial p^f}\left(\xi\rho^l + (1-\xi)\,\rho^g\right) &= \\
\frac{1-\xi}{k^g} &\rightsquigarrow \\
\mathcal{D}_B^f = 0 \quad \square\,. &
\end{aligned} \tag{2.60}$$

The last part of dissipation, $\mathcal{D}^v$, can be reformulated as

$$\begin{aligned}
\mathcal{D}^v &= \\
n^f\boldsymbol{\tau}^f : \boldsymbol{l}^f &= \\
n^f\boldsymbol{\tau}^f : \boldsymbol{D}^f &= \\
n^f\left(\left(\lambda^f \mathrm{tr}\left(\boldsymbol{D}^f\right)\mathbf{1} + 2\mu^f\boldsymbol{D}^f\right)\right) : \boldsymbol{D}^f &= \\
n^f\left(\left(\lambda^f + \frac{2}{3}\mu^f\right)\left(\mathrm{tr}\left(\boldsymbol{D}^f\right)\right)^2 + 2\mu^f\boldsymbol{D}^f_{dev} : \boldsymbol{D}^f_{dev}\right) &\geqslant 0\,,
\end{aligned} \tag{2.61}$$

where $\boldsymbol{D}^f$ is the symmetrical part of $\boldsymbol{l}^f$, and $\boldsymbol{D}^f_{dev}$ is the deviatoric part of $\boldsymbol{D}^f$. λ and μ refer to Lamé first parameter and Lamé second parameter, respectively. It is obvious that all terms in Equation (2.61) are positive or zero, so we can conclude that $\mathcal{D}^v$ is larger than or equal to zero.

2.2 Current status of process modeling

The purpose of process modeling is to give engineers and scientists better insight into the flow pattern, the extent of curing, and the response of fiber preforms. By implementing process models, process engineers can find the best parameters of the processing without conducting experiments. The model can reveal the performance and outcome of different mold designs and save the expense and time of fabricating and testing every case [4].

Generally, the modeling starts with the problem definition. In this stage, we need to define and abstract the physical process, identify the important parameters, and consider the boundary conditions and so on. Next, we should use fundamental physical laws and empirical observations to formulate the mathematical expressions of the defined problem. To reduce the complexities of mathematical equations, we have to simplify the model by making suitable assumptions. The obtained equations are usually a system of coupled nonlinear partial differential equations. The finite difference, boundary element method, control volume finite element method, and Galerkin finite element method are among the means to find solutions numerically. The main challenges for solving the equation system are reliability, stability, portability, and efficiency. Once the model is developed, the verification and validation need to be implemented. The verification tells whether or not the model gives correct solutions. On the other hand, the validation allows checking if there are ignored phenomena in the course of the process. Moreover, through the validation, we will know how well the model matches physics in the process mathematically.

Between the late 80s and early 90s, Chan and Hwang [11] started to solve the pressure distribution in the RTM process based on Darcy's law, which describes the fluid transferring in porous media. Fracchia et al., [12] employed the control volume finite element method (CVFEM) together with the concept of volume of fraction (VOF) to simulate the mold filling in the RTM process using conforming finite elements. Since then, many results following this approach have been published, e.g., [13, 14, 15, 16, 17, 18, 19, 20, 21, 22]. The modified CVFEM, e.g., [23, 24, 25], have been proposed as well. The boundary element method (BEM), e.g., [26, 27], and the smoothed particle hydrodynamics (SPH) method, e.g., [28, 29, 30] are also among the methods of modeling.

Regarding the flow front tracking, the level set method, e.g., Soukane and Trochu [31] or Gantois et al., [32], natural element method (NEM) [33] and discontinuous Galerkin method (DGM) [34] are developed to improve the flow front tracking. Another interesting study has been done recently by Dammann and Mahnken [35], who used the phase-field models to model the RTM process. Besides, Wu and Larsson [36] proposed a model using the degree of saturation concept to describe the flow front.

Another approach is to consider the flow as a dual-scale flow. The intra-tow flow can be treated as delayed infiltration of tows, which can be modeled as sinks of inter-tow flow,

as described in [37, 38, 39, 40, 41, 42, 43]. In addition, a multiscale algorithm has been reported by Tan and Pillai [44].

Researchers also classify the resin flow to saturated and unsaturated flow. Hammami and Gebart [45], Correia et al. [46], and Fracassi and Donadon [47] reported 1-D analytical models of the saturated flow. Various unsaturated flow models are also reported, e.g., [48, 49, 50]. Some researchers formulated multiphase flow equations with the absence of capillary pressure [51, 31]; others include the capillary effect, e.g., [52, 53, 54, 55, 36, 56]. Apart from the single-phase fluid modeling, e.g., [11], the gas-liquid mixed fluid is also attractive, e.g., the three-phase porous media models [57, 58, 59, 60] account for the integration of gas, liquid resin, and solid fiber networks.

Besides, various studies on preform response were reported by researches e.g., [61, 62, 63, 64, 65, 46, 66, 67, 68, 69, 70, 47, 71, 72].

On the other hand, researchers also reported various of cure kinetics models e.g., [73, 74, 75, 76, 77, 78, 79, 80, 81, 82, 83, 84, 85]. In addition, the chemo-rheological models were also proposed e.g., [86, 87, 88, 89, 90, 91, 92, 93]. Moreover, the simulations of the non-isothermal process that considers the exothermic resin reactions have been carried out, e.g., [94, 95, 96, 97, 98].

3 Summary of appended papers

Paper A: **Homogenized free surface flow in porous media for wet-out processing**

The paper proposes a mathematical model for simulating the wet-out processing, e.g., the infusion stage of the RTM process. Based on the theory of porous media, we use the concept of volume fraction to distinguish the constituents of solid fiber and fluid. Then the degree of saturation is utilized to separate the fluid as air and liquid resin. By introducing the capillary effect between gas and liquid resin, we employ the concept of relative permeability. It has been justified that the existence of the relative permeability plays a significant role in obtaining a discontinuous-like flow front, which has been ignored in the previous study [58]. Further, air and resin are homogenized as a mixed fluid, which is characterized by the mixed pressure. From the homogenization, we extend the standard Darcy's law. The flow velocity is not only determined by the pressure gradient, but the gradient of the saturation as well. Moreover, when the capillary effect is small enough, the extended Darcy's law will turn back to the standard one. The governing equations are then derived from the mass conservation principle. The saturation equation is obtained from the mass balance of the liquid resin, while the pressure equation is derived from the homogenized fluid mass conservation. To solve this highly non-linear and coupled equation system, we employed the finite element method with the staggered approach. What's more, the severe fluctuation of the saturation degree solution is noticed. The reason for this problem is because the saturation equation turns out to be a convection dominated formulation. To enhance the stability, we adopt the Streamline-Upwind/Petrov-Galerkin (SUPG) technique in the original formulation.

In this paper, the expression of Darcy's velocity has been proposed specifically as,

$$\begin{aligned} \boldsymbol{v}^{dl} &:= n^l \boldsymbol{v}^{rl} = -\boldsymbol{K}^l \boldsymbol{\nabla} p^l \ , \\ \boldsymbol{v}^{dg} &:= n^g \boldsymbol{v}^{rg} = -\boldsymbol{K}^g \boldsymbol{\nabla} p^g \ , \text{ and} \\ &\left\{ \boldsymbol{K}^\alpha = \frac{\hat{\boldsymbol{k}} k_{r\alpha}}{\mu_\alpha} \right\}_{\alpha=l,g} \ , \end{aligned} \tag{3.1}$$

where $\hat{\boldsymbol{k}}$ is the intrinsic permeability of the fiber preform, $k_{r\alpha}$ denotes the relative permeability by Burdine [99] and μ_α represents the viscosity. We studied the influence of the relative permeability as shown in Figure 3.1 . The relative permeability gives rise to more abrupt responses of pressure and degree of saturation at the flow front.

The comparison between the presented model and the previous model has been made in Figure 3.2. The improved model in **Paper A** gives better match with the analytical reference.

Two 2-D numerical examples were made to demonstrate the simulations of the RTM process. From Figure 3.3 and Figure 3.4, it is evident that the flow fronts are very narrow and they localize only in a few elemental widths, which reflects the discontinuity.

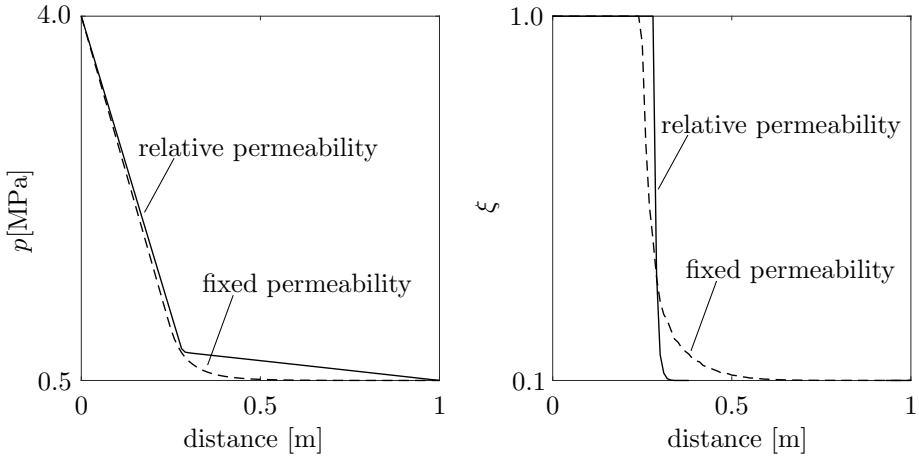

Figure 3.1: The comparison between the model with relative permeability and fixed permeability.

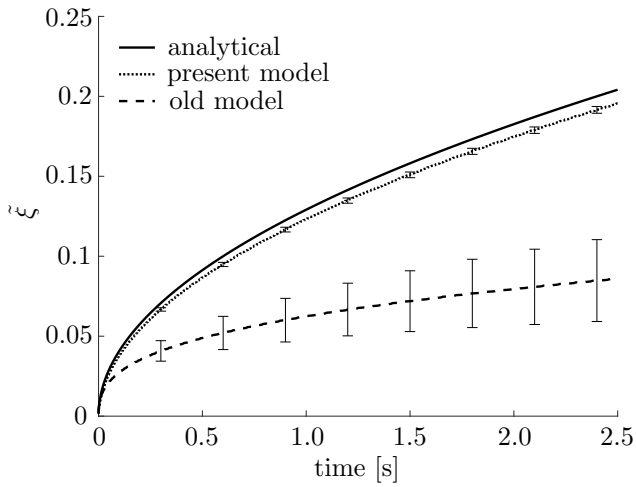

Figure 3.2: The comparison of the global saturation degree between analytical solution, the present model and the reference model [58] with 1000 elements meshing. The bars in the figure illustrate the L^2–norm errors against the analytical results.

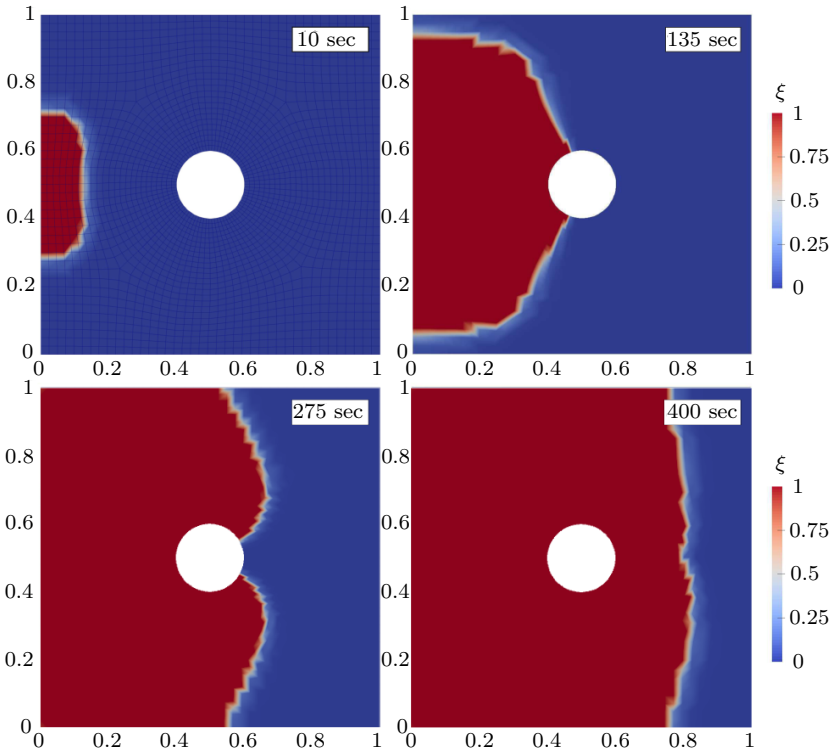

Figure 3.3: Resin flow locations at 10 s, 135 s, 275 s and 400 s after the infusion started.

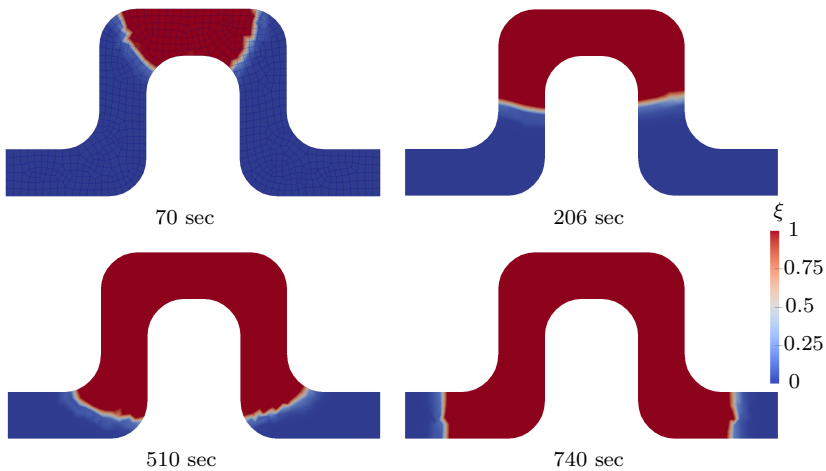

Figure 3.4: Resin flow locations at 70 s, 206 s, 510 s and 740 s after the infusion started.

Paper B: **A shell model for resin flow and preform deformation in thin-walled composite manufacturing processes**

In **Paper B**, we continuously extend the contribution from **Paper A**. The fiber preform deformation is modeled together with the flow in this work. Some liquid composite molding processes, e.g., the vacuum assisted resin transfer molding (VARTM) process, have the problem of thickness variation on the final products. This is due to the fiber preform deforms during the infusion stage caused by the fluid pressure unevenly distributed. Besides, the VARTM process is usually used to produce large-scale composite parts, which are typically thin-walled components. Since the components are thin enough to ignore the variation of the through-thickness flow, we can reduce the problem from the full 3-D case to a 2-D shell-like problem. To simplify the 3-D flow, we introduce the planar projection tensor from the local monoclinic coordinates to project the flow onto the preform surface. Due to the pressure difference between the external environment and the internal fluid, the fiber preform expansion and compaction are interested. Based on the shell assumption, we propose a kinematic model to catch the normal directional stretch of the preform. We utilize the modified packing law in the linear momentum balance equation to obtain an explicit formation of the preform stretch. Thus the deformation will be illustrated by the stretch that only depends on the mixed pressure from the homogenized flow. Given this simplification, we dramatically reduce the computational effort but can still capture the physics during the process.

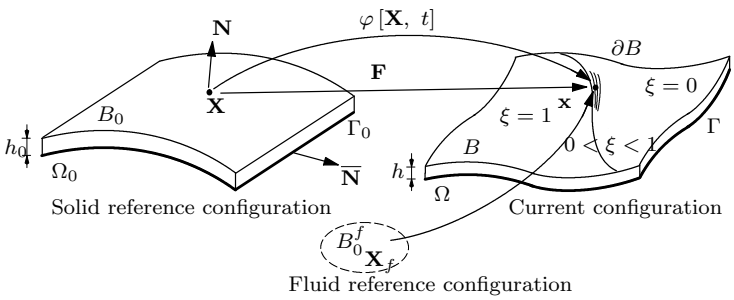

Figure 3.5: The reference and current configuration of a partial-saturated deformable thin-walled preform. The thickness of the undeformed thin-walled preform is h_0 and after deformation the thickness turns to h. B_0 and B denote the region of undeformed and deformed preform respectively, and the preform bottom is named as Ω_0 (or Ω). In the figure, $\boldsymbol{N}$ is the unit normal of Ω_0, whereas $\bar{\boldsymbol{N}}$ is the outward unit normal of the boundary line Γ_0.

Regarding the LCM process of a deformable thin-walled preform, to represent the deformation of the thin-walled preform, we modify the kinematics in Section 2.1.2 and use the stretch λ to represent the ratio between the thicknesses of the deformed and undeformed preform, which can be expressed as

$$\lambda = \frac{h}{h_0}. \tag{3.2}$$

The deformation gradient of the preform is simplified to

$$\boldsymbol{F} = \mathbf{1} + (\lambda - 1)\boldsymbol{N} \otimes \boldsymbol{N} \ , \tag{3.3}$$

where the normal stretch λ is equal to the Jacobian of the deformation gradient, $\lambda = J = \det \boldsymbol{F}$.

Based on this shell kinematics, we obtained the explicit stretch expression as

$$\boxed{\lambda = \left(1 + \frac{p^a - p^f}{k^s E (n_0^s)^m}\right)^{-1/m}} \ , \tag{3.4}$$

where p^a is the atomspheric pressure, k^s and m are parameters in Toll's packing law, and the variable E represents the elastic Young's modulus of fibers.

Another study made in **Paper B** is the limitation of the thin-walled assumption. Figure 3.6 shows that the percent error, $\delta = \left| \left(\hat{\boldsymbol{\xi}}_{plane} - \hat{\boldsymbol{\xi}}_{shell} \right) / \hat{\boldsymbol{\xi}}_{shell} \right| \times 100\%$, decreases linearly as the preform thickness decreases. When the ratio t/L is reduced below 6%, the influence of the through-thickness flow is significantly reduced. A numerical example is

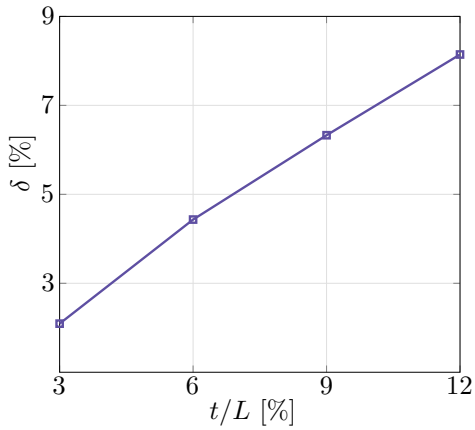

Figure 3.6: The differences of the global saturation degree between the plane and shell model.

made to illustrate the model. Figure 3.7 plots the resin flow patterns during the infusion stage. The red regions represent the full-saturated parts of the preform; and the blue regions indicate the dry parts; the gradients between red and blue illustrate the process zone, where the flow front locates. It is obvious to observe that as the resin flows into the preform, the preform deforms correspondingly.

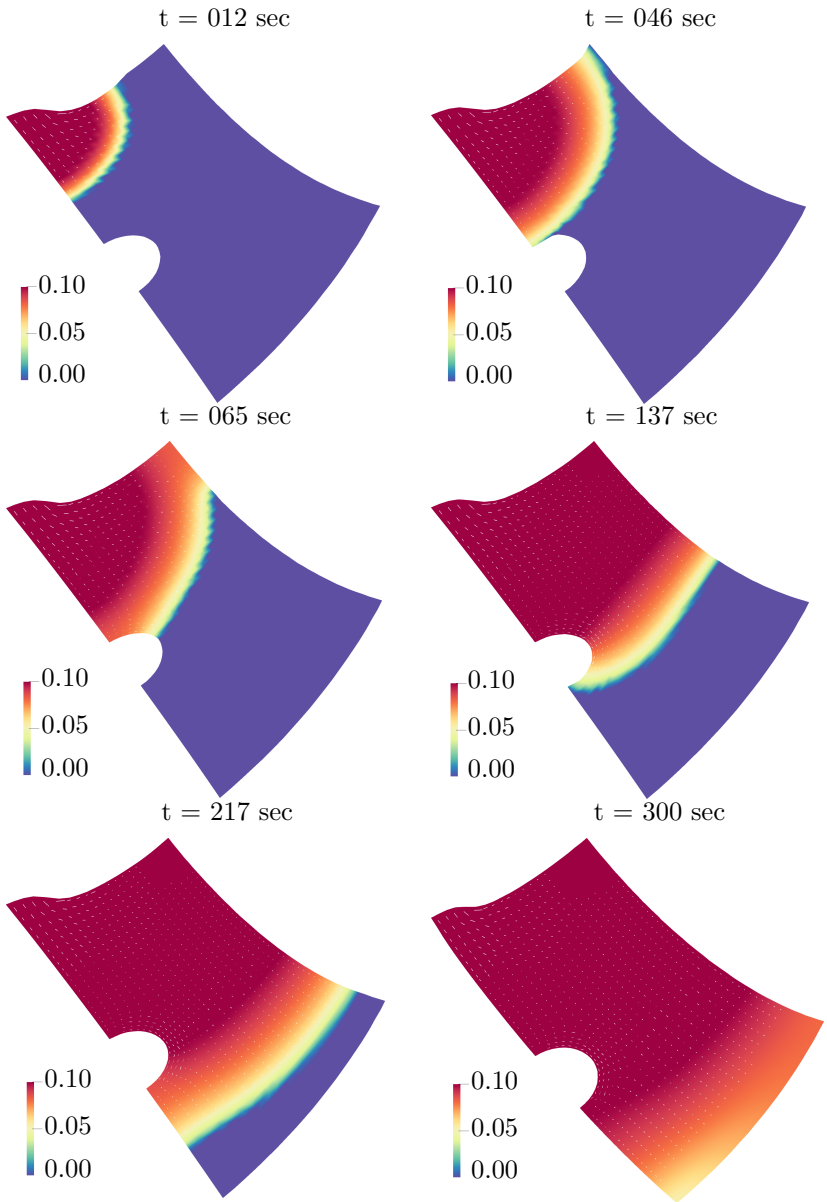

Figure 3.7: Resin flow pattern and prefrom deformation.

Paper C: **Modeling and experimental validation of the VARTM process for thin-walled preforms**

Paper B proposed a shell model for simulating resin flow and preform deformation in the LCM process of thin-walled preforms. To verify and validate the shell model, we experimented with the VARTM process. The experimental setup is depicted in Figure 3.8. First, eight layers of NCF are stacked on a flat aluminum mold (1 m $\times$ 1 m), following the $[-45/45/90/0]_s$ layup, to assemble the fibrous preform (22 cm $\times$ 38 cm). Then, on top of the preform, a layer of peel ply is placed. Because the preform is thin (6.5 mm) compared with other dimensions, the distribution layer is ignored. A helical tube is placed at the inlet of the mold. The inlet tube connects to the resin reservoir, and the outlet tube is connected to the vacuum pump. Finally, the mold is covered by a vacuum bag and sealed with tacky tapes around all edges of the preform. When the VARTM experiment setup is ready, the Digital Image Correlation (DIC) system from GOM Aramis® is installed on top of the mold to carry out the in situ monitoring during the infusion process.

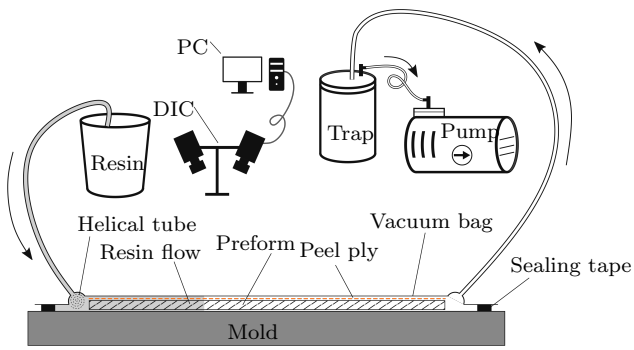

Figure 3.8: The VARTM experiment setup.

In Figure 3.9, the simulation results show good agreements with the experimental results, especially for the locations of the maximum relaxation and lubrication. From 29 s to 302 s, the relaxation from the simulation almost keeps in line with the experiment. However, at 500 s and 800 s, there are some deviations between the simulation and the experiment. The neglected bending of the preform may cause deviations. Nevertheless, the model successfully mimics the preform relaxation mechanism and lubrication effects. In summary, the present model, with the assumptions of in-plane flow and shell kinematics, provides good predictions of the preform deformation in the VARTM process of thin-walled preforms and needs less computational effort.

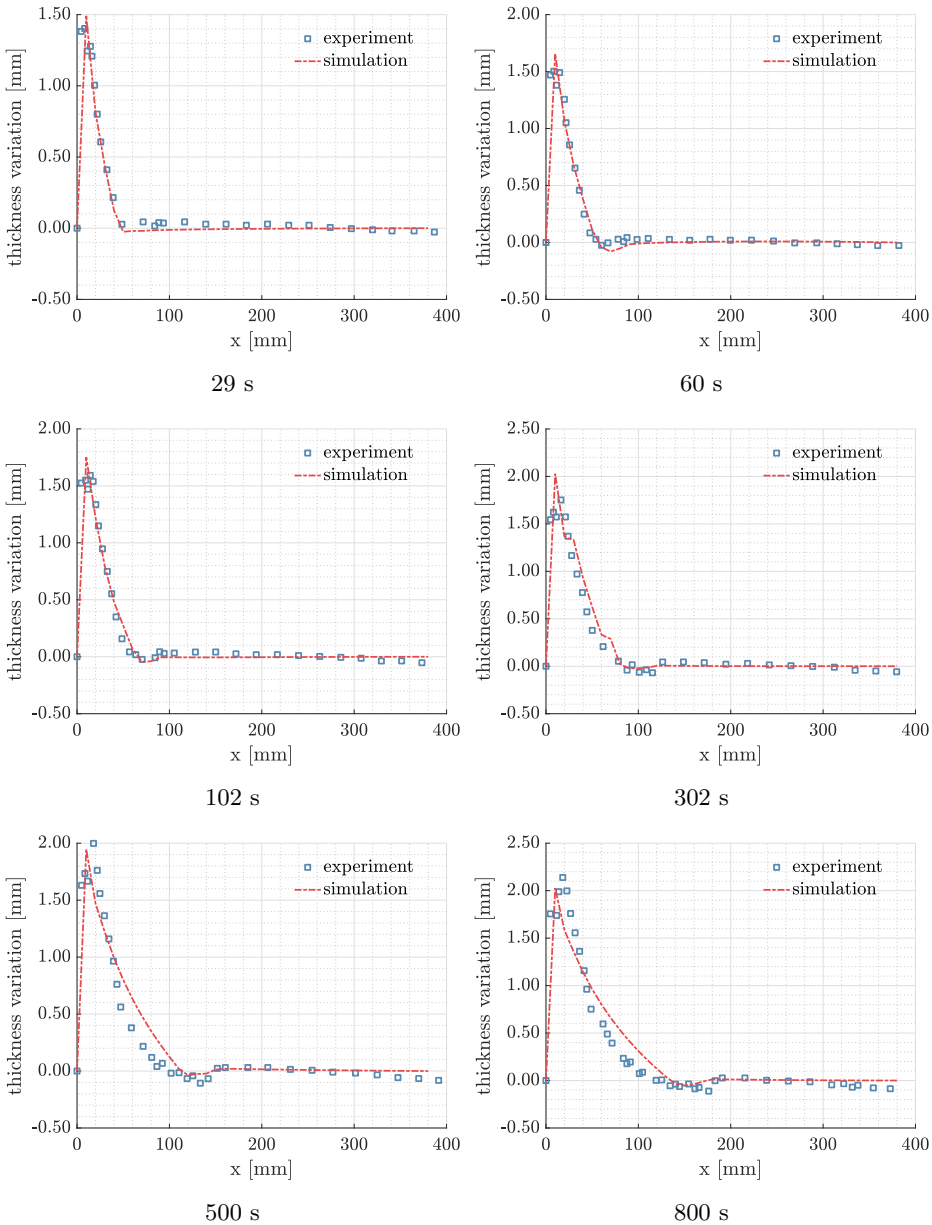

Figure 3.9: The comparison of thickness variation between the experiment and simulation.

Paper D: **A preform deformation and resin flow coupled model including the cure kinetics and chemo-rheology for the VARTM process**

Paper A, **Paper B**, and **Paper C** are only aimed at the infusion stage. However, in fact, resin flow development, heat transfer, and resin curing are strongly interrelated. The exothermic reactions increase resin temperature – additionally change the viscosity, which in turn affects the flow filling pattern. Moreover, the degree of cure upon the completion of the infusion stage contributes to the initial conditions for the curing stage. The reduction of the process cycle time may benefit from the adequate control of the temperature and initialization of polymerization. In **Paper D**, the in-plane two-phase flow and the shell preform model are combined with heat transfer, cure kinetics, and chemo-rheology in the simulation of the thin-walled VARTM process. The resin reaction Equation (3.5) and the heat transfer Equation (3.6) are extended to include the fiber preform response.

$$\boxed{n^l \frac{\partial c}{\partial t} + n^l \boldsymbol{v}^s \cdot \boldsymbol{\nabla} c + \boldsymbol{v}^{dl} \cdot \boldsymbol{\nabla} c = \boldsymbol{\nabla} \cdot \left(n^l \left(\boldsymbol{D}_e + \boldsymbol{D}_D \right) \boldsymbol{\nabla} c \right) + n^l G} \,, \tag{3.5}$$

where c is the degree of cure, and G is obtained from the Kamal and Sourour [73] autocatalytic model. $\boldsymbol{D}_e$ is the effective diffusivity tensor, and $\boldsymbol{D}_D$ is the hydrodynamic dispersion tensor.

$$\boxed{\begin{aligned} \hat{c}_p \frac{\partial T}{\partial t} + \hat{c}_p \boldsymbol{v}^s \cdot \boldsymbol{\nabla} T + \rho^f c_p^f \boldsymbol{v}^{df} \cdot \boldsymbol{\nabla} T = \\ n^f \boldsymbol{\nabla} \cdot \left(\boldsymbol{k}^f \cdot \boldsymbol{\nabla} T \right) + n^s \boldsymbol{\nabla} \cdot \left(\boldsymbol{k}^s \cdot \boldsymbol{\nabla} T \right) + n^f \Delta H G \end{aligned}} \,, \tag{3.6}$$

where the homogenized specific heat $\hat{c}_p = n^s \rho^s c_p^s + n^f \rho^f c_p^f$. c_p^f and c_p^s are the specific heats of the fluid and fiber, respectively. $\boldsymbol{k}^f$ and $\boldsymbol{k}^s$ are the conductivity of the fluid and preform, respectively. Additionally, the reaction heat of resin is denoted as ΔH.

Equation (3.5) and Equation (3.6) belong to the convection-diffusion equations and are solved by the Galerkin finite element method. The solutions are plotted in Figure 3.10 and Figure 3.11, respectively. It is obvious that the initial temperatures influence the degree of cure and the temperature of resin dramatically.

The holistic simulation of the non-isothermal VARTM process has been done efficiently. Figure 3.12 shows the filling time and the maximum degree of cure for each given initial temperature. When the initial temperature varies from 298 K to 373 K, the filling out time drops 68.5%. On the contrary, the degree of cure increases three times. In this regard, the infusion process is accelerated by increasing the initial temperature. However, when the initial temperature keeps rising to 398 K, the filling out time jumps dramatically to 278 seconds. In addition, the degree of cure reaches 0.839, which is too high compared with the usual VARTM process. In conclusion, there is a window of the processing temperature that can shorten the time of the infusion stage.

Paper D provides a numerical tool that can be used for optimizing the process parameters and the design of the mold, such as the initial temperature, the vacuum level, and the position of the inlet and outlet. What is more, the proposed model can check the compatibility of a resin system for a given infusion task without relying on the experience and "trial and error" approaches. Finally, the residual thermal stress can be computed based on the thermal condition obtained from this model.

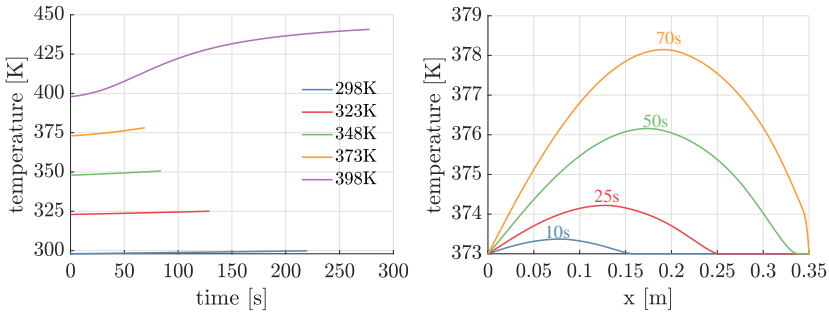

(a) (b)

Figure 3.10: (a) The changes of temperature at flow fronts. (b) The profiles of temperature along the centerline.

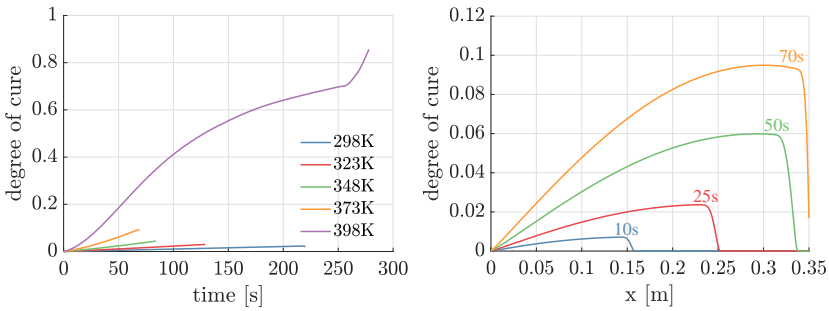

(a) (b)

Figure 3.11: (a) The changes of degree of cure at flow fronts. (b) The profiles of degree of cure along the centerline.

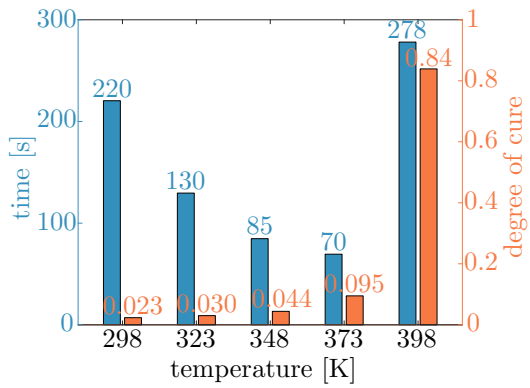

Figure 3.12: The filling out time and maximum degree of cure at different initial temperatures.

4 Concluding remarks and future work

Nowadays, the trial-and-error is still the primary solution among manufactures for developing high-performance composite materials, e.g., for space applications. The energy used on trails, the wasted cost from failing, and the spent time is out of affordability of small size manufacturers. It leads to both a negative impact on sustainable development and markedly less competitive. To improve the situation, we need help from numerical simulations and predictions. By using virtual numerical experiments, the process engineers can design and control process parameters and optimize the mold shape. Finally, the quality of products can be improved, the processing cost can be reduced, and the eco-friendly can be enhanced.

In this thesis, we focused on the liquid composite molding processes, e.g., the RTM and VARTM processes. The proposed mathematical model based on the theory of porous media and Darcy flow can predict the resin flow movement. We have noticed that the saturation degree curves show a discontinuous jump at flow fronts when the capillary pressure and relative permeability are considered. This may give us hints to model the saturation degree based on a discontinuous method, e.g., the Discontinuous Galerkin Method in [34] or the phase-field approach [35]. It is efficient to model the resin flow as Darcy flow when the information of dual-scale flow are absent, which are essential for modeling of void formation. The intra-tow flow can be treated as delayed infiltration of tows, which can be modeled as sinks of inter-tow flow, as described in [42, 43]. Last but not least, due to the orientations of the fiber bundles, the PMC materials usually have anisotropic permeability, e.g., [100]. The relevant works could also be interesting.

The response of the fiber preform is usually complicated and challenging to model. In this thesis, we make an assumption of the shell kinematics to abstract the primary phenomenon of the thin-walled fiber preform deformation. In this regard, the problem size is dramatically decreased, and it makes the model possible to be used in the industry. However, from Figure 3.9, we notice that the bending effect influences the accuracy. Thus, it is also important to define the constitutive relation of the fiber preform, e.g., free energy ψ^s, which can give a more accurate response of the preform deformation.

Besides, heat transfer, cure kinetics, and rheological models are also studied to investigate the effects of the exothermic polymerization during the VARTM process. When the highly convective non-isothermal flow of the reactive resin moves into the preform, the cure of resin generates heat and accelerates the process of cross-linking. Accordingly, the viscosity and the flow velocity increase or decrease depending on the temperature and the degree of cure. On the other hand, the compaction and expansion of the preform change the structure and permeability of the preform, which affects the infusion speed. The simulation shows the existence of a temperature window that the infusion process can be speeded up dramatically. Moreover, the post filling stage can be modeled based on the present works to analyze the stress status and final shape of the preform.

In conclusion, the present work provides a numerical solution to composite manufacturers as a CAE tool. The tool can help the industry to optimize their process designs, e.g., 1) design of appropriate tool compensation; 2) modification of process parameters to reduce the residual stress and the deformation; 3) savings of material, time, and cost; 4)

predictive tool for manufacturability; 5) design of the locations of gates and vents, and the list goes on.

References

[1] L. E. Asp, M. Johansson, G. Lindbergh, J. Xu, and D. Zenkert. Structural battery composites: a review. en. *Funct. Compos. Struct.* **1**.4 (Nov. 2019), 042001. ISSN: 2631-6331. DOI: 10.1088/2631-6331/ab5571.

[2] B. T. Åström. *Manufacturing of Polymer Composites*. Chapman & Hall, 1997. 500 pp. ISBN: 978-0-412-81960-5.

[3] S. G. Advani and K.-T. Hsiao. *Manufacturing Techniques for Polymer Matrix Composites (PMCs)*. Elsevier, July 18, 2012. 512 pp. ISBN: 978-0-85709-625-8.

[4] S. G. Advani and E. M. Sozer. *Process modeling in composites manufacturing*. CRC press, 2010.

[5] R. Woltmann. *Beitrage zur Hydraulischen architectur*. Johann Christian Dieterich, 1794.

[6] M Delesse. Pour déterminer la composition des roches. Annales des mines. *4. séries* **13** (1848), 379–388.

[7] A. Fick. Ueber diffusion. *Annalen der Physik* **170**.1 (1855), 59–86.

[8] J. Stefan. *Über das Gleichgewicht und die Bewegung, insbesondere die Diffusion von Gasgemengen*. Universitätsbibliothek Johann Christian Senckenberg, 2007.

[9] W. G. Gray and S. M. Hassanizadeh. Paradoxes and Realities in Unsaturated Flow Theory. *Water Resources Research* **27**.8 (Aug. 1991), 1847–1854. ISSN: 1944-7973. DOI: 10.1029/91WR01259.

[10] B. D. Coleman and W. Noll. The thermodynamics of elastic materials with heat conduction and viscosity. *Archive for rational mechanics and analysis* **13**.1 (1963), 167–178.

[11] A. W. Chan and S.-T. Hwang. Modeling of the impregnation process during resin transfer molding. *Polymer Engineering & Science* **31**.15 (Aug. 1991), 1149–1156. ISSN: 1548-2634. DOI: 10.1002/pen.760311512.

[12] C. A. Fracchia, J. Castro, and C. L. Tucker. "A finite element/control volume simulation of resin transfer mold filling". *Proceedings of the American society for composites, fourth technical conference*. 1989, pp. 157–166.

[13] M. V. Bruschke and S. G. Advani. A finite element/control volume approach to mold filling in anisotropic porous media. *Polymer composites* **11**.6 (1990), 398–405.

[14] F. Trochu, R. Gauvin, and D.-M. Gao. Numerical analysis of the resin transfer molding process by the finite element method. *Advances in Polymer Technology* **12**.4 (Dec. 1993), 329–342. ISSN: 1098-2329. DOI: 10.1002/adv.1993.060120401.

[15] V. R. Voller and S. Peng. An algorithm for analysis of polymer filling of molds. *Polymer Engineering & Science* **35**.22 (Nov. 1995), 1758–1765. ISSN: 1548-2634. DOI: 10.1002/pen.760352205.

[16] R. S. Maier, T. F. Rohaly, S. G. Advani, and K. D. Fickie. A Fast Numerical Method for Isothermal Resin Transfer Mold Filling. *International Journal for Numerical Methods in Engineering* **39**.8 (Apr. 1996), 1405–1417. ISSN: 1097-0207. DOI: 10.1002/(SICI)1097-0207(19960430)39:8<1405::AID-NME910>3.0.CO;2-S.

[17] M. L. Diallo, R. Gauvin, and F. Trochu. Experimental analysis and simulation of flow through multi-layer fiber reinforcements in liquid composite molding. *Polym Compos* **19**.3 (June 1998), 246–256. ISSN: 1548-0569. DOI: 10.1002/pc.10097.

[18] S. T. Lim and W. I. Lee. An analysis of the three-dimensional resin-transfer mold filling process. *Composites Science and Technology* **60**.7 (May 2000), 961–975. ISSN: 02663538. DOI: 10.1016/S0266-3538(99)00160-8.

[19] B. Minaie, Y. F. Chen, and A. M. Mescher. A Methodology to Obtain a Desired Filling Pattern during Resin Transfer Molding. *Journal of Composite Materials* **36**.14 (July 2002), 1677–1692. ISSN: 0021-9983. DOI: 10.1177/0021998302036014165.

[20] J. Samir, J. Echaabi, and M. Hattabi. Numerical algorithm and adaptive meshing for simulation the effect of variation thickness in resin transfer molding process. *Composites Part B-Engineering* **42**.5 (July 2011), 1015–1028. ISSN: 1359-8368. DOI: 10.1016/j.compositesb.2011.03.027.

[21] V. R. Voller and Y. F. Chen. Prediction of Filling Times of Porous Cavities. *International Journal for Numerical Methods in Fluids* **23**.7 (Oct. 1996), 661–672. ISSN: 1097-0363. DOI: 10.1002/(SICI)1097-0363(19961015)23:7<661::AID-FLD448>3.0.CO;2-E.

[22] B. Yang, T. Jin, J. Li, and F. Bi. Simulating the resin flow and stress distributions on mold tools during compression resin transfer molding. *Journal of Reinforced Plastics and Composites* **33**.14 (July 2014), 1316–1331. ISSN: 0731-6844. DOI: 10.1177/0731684414528831.

[23] F. R. Phelan. Simulation of the injection process in resin transfer molding. *Polym Compos* **18**.4 (Aug. 1997), 460–476. ISSN: 1548-0569. DOI: 10.1002/pc.10298.

[24] M. K. Kang and W. I. Lee. A flow-front refinement technique for the numerical simulation of the resin-transfer molding process. *Composites Science and Technology* **59**.11 (Aug. 1999), 1663–1674. ISSN: 0266-3538. DOI: 10.1016/S0266-3538(99)00029-9.

[25] S. C. Joshi, Y. C. Lam, and X. L. Liu. Mass conservation in numerical simulation of resin flow. *Composites Part A: Applied Science and Manufacturing* **31**.10 (Oct. 2000), 1061–1068. ISSN: 1359-835X. DOI: 10.1016/S1359-835X(00)00067-1.

[26] H.-S. Lee, H.-C. Sin, and S.-G. Kim. Iterative boundary pressure reflection method for the simulation of injection mold filling. *Polymer Engineering & Science* **30**.23 (Dec. 1990), 1513–1522. ISSN: 1548-2634. DOI: 10.1002/pen.760302305.

[27] M.-K. Um and W. I. Lee. A study on the mold filling process in resin transfer molding. *Polym Eng Sci* **31**.11 (June 1991), 765–771. ISSN: 1548-2634. DOI: 10.1002/pen.760311102.

[28] M. Sawley, P. Cleary, and J. Ha. Modelling of flow in porous media and resin transfer moulding using smoothed particle hydrodynamics (1999).

[29] C. Binetruy and S. G. Advani. Foam Core Deformation During Liquid Molding of Sandwich Structures: Modeling and Experimental Analysis. *Jnl of Sandwich Structures & Materials* **5**.4 (Oct. 2003), 351–375. ISSN: 1099-6362. DOI: 10.1177/109963603027909.

[30] S. Comas-Cardona, P. Groenenboom, C. Binetruy, and P. Krawczak. A generic mixed FE-SPH method to address hydro-mechanical coupling in liquid composite moulding processes. *Composites Part A: Applied Science and Manufacturing* **36**.7

(July 2005), 1004–1010. ISSN: 1359-835X. DOI: 10.1016/j.compositesa.2004.11.009.

[31] S. Soukane and F. Trochu. Application of the level set method to the simulation of resin transfer molding. *Composites Science and Technology* **66**.7 (2006), 1067–1080. ISSN: 0266-3538. DOI: https://doi.org/10.1016/j.compscitech.2005.03.001.

[32] R. Gantois, A. Cantarel, G. Dusserre, J.-N. Félices, and F. Schmidt. Numerical Simulation of Resin Transfer Molding Using BEM and Level Set Method. *Int J Mater Form* **3**.1 (Apr. 1, 2010), 635–638. ISSN: 1960-6214. DOI: 10.1007/s12289-010-0850-9.

[33] M. A. Martínez, E. Cueto, M. Doblaré, and F. Chinesta. Natural element meshless simulation of flows involving short fiber suspensions. *Journal of Non-Newtonian Fluid Mechanics* **115**.1 (Oct. 2003), 51–78. ISSN: 0377-0257. DOI: 10.1016/S0377-0257(03)00171-X.

[34] J. Remacle, J. Flaherty, and M. Shephard. An Adaptive Discontinuous Galerkin Technique with an Orthogonal Basis Applied to Compressible Flow Problems. *SIAM Rev.* **45**.1 (Jan. 2003), 53–72. ISSN: 0036-1445. DOI: 10.1137/S00361445023830.

[35] C. Dammann and R. Mahnken. Simulation of a resin transfer molding process using a phase field approach within the theory of porous media. *Composites Part A: Applied Science and Manufacturing* **120** (May 1, 2019), 147–160. ISSN: 1359-835X. DOI: 10.1016/j.compositesa.2019.02.022.

[36] D. Wu and R. Larsson. Homogenized free surface flow in porous media for wet-out processing. en. *International Journal for Numerical Methods in Engineering* **1**.17 (May 2018). ISSN: 00295981. DOI: 10.1002/nme.5812.

[37] K. M. Pillai and S. G. Advani. A Model for Unsaturated Flow in Woven Fiber Preforms during Mold Filling in Resin Transfer Molding. en. *Journal of Composite Materials* **32**.19 (Oct. 1998), 1753–1783. ISSN: 0021-9983. DOI: 10.1177/002199839803201902.

[38] F. D. Dungan and A. M. Sastry. Saturated and Unsaturated Polymer Flows: Microphenomena and Modeling. en. *Journal of Composite Materials* **36**.13 (July 2002), 1581–1603. ISSN: 0021-9983. DOI: 10.1177/0021998302036013179.

[39] P. Simacek and S. G. Advani. A numerical model to predict fiber tow saturation during liquid composite molding. *Composites Science and Technology* **63**.12 (Sept. 2003), 1725–1736. ISSN: 0266-3538. DOI: 10.1016/S0266-3538(03)00155-6.

[40] N. Kuentzer, P. Simacek, S. G. Advani, and S. Walsh. Correlation of void distribution to VARTM manufacturing techniques. *Composites Part A: Applied Science and Manufacturing* **38**.3 (Mar. 2007), 802–813. ISSN: 1359-835X. DOI: 10.1016/j.compositesa.2006.08.005.

[41] F. Zhou, J. Alms, and S. G. Advani. A closed form solution for flow in dual scale fibrous porous media under constant injection pressure conditions. *Composites Science and Technology* **68**.3 (Mar. 2008), 699–708. ISSN: 0266-3538. DOI: 10.1016/j.compscitech.2007.09.010.

[42] H. Tan and K. M. Pillai. Fast liquid composite molding simulation of unsaturated flow in dual-scale fiber mats using the imbibition characteristics of a fabric-based

unit cell. en. *Polymer Composites* **31**.10 (2010), 1790–1807. ISSN: 1548-0569. DOI: 10.1002/pc.20971.

[43] L. Gascón, J. A. García, F. LeBel, E. Ruiz, and F. Trochu. Numerical prediction of saturation in dual scale fibrous reinforcements during Liquid Composite Molding. *Composites Part A: Applied Science and Manufacturing* **77** (Oct. 2015), 275–284. ISSN: 1359-835X. DOI: 10.1016/j.compositesa.2015.05.019.

[44] H. Tan and K. M. Pillai. Multiscale modeling of unsaturated flow in dual-scale fiber preforms of liquid composite molding I: Isothermal flows. *Composites Part A: Applied Science and Manufacturing* **43**.1 (Jan. 2012), 1–13. ISSN: 1359-835X. DOI: 10.1016/j.compositesa.2010.12.013.

[45] A. Hammami and B. R. Gebart. Analysis of the vacuum infusion molding process. en. *Polymer Composites* **21**.1 (2000), 28–40. ISSN: 1548-0569. DOI: 10.1002/pc.10162.

[46] N. C. Correia, F. Robitaille, A. C. Long, C. D. Rudd, P. Šimáček, and S. G. Advani. Analysis of the vacuum infusion moulding process: I. Analytical formulation. *Composites Part A: Applied Science and Manufacturing* **36**.12 (Dec. 2005), 1645–1656. ISSN: 1359-835X. DOI: 10.1016/j.compositesa.2005.03.019.

[47] F. T. Fracassi and c V. Simulation of vacuum assisted resin transfer molding process through dynamic system analysis. en. *Journal of Composite Materials* **52**.27 (Nov. 2018), 3759–3771. ISSN: 0021-9983. DOI: 10.1177/0021998318770000.

[48] K. M. Pillai. Modeling the Unsaturated Flow in Liquid Composite Molding Processes: A Review and Some Thoughts. en. *Journal of Composite Materials* **38**.23 (Dec. 2004), 2097–2118. ISSN: 0021-9983. DOI: 10.1177/0021998304045585.

[49] M. Nordlund and V. Michaud. Dynamic saturation curve measurement for resin flow in glass fibre reinforcement. *Composites Part A: Applied Science and Manufacturing* **43**.3 (Mar. 2012), 333–343. ISSN: 1359-835X. DOI: 10.1016/j.compositesa.2011.12.001.

[50] V. Michaud. A Review of Non-saturated Resin Flow in Liquid Composite Moulding processes. en. *Transport in Porous Media* **115**.3 (Dec. 2016), 581–601. ISSN: 1573-1634. DOI: 10.1007/s11242-016-0629-7.

[51] K.-T. Hsiao, R. Mathur, S. G. Advani, J. W. Gillespie, and B. K. Fink. A Closed Form Solution for Flow During the Vacuum Assisted Resin Transfer Molding Process. en. *Journal of Manufacturing Science and Engineering* **122**.3 (2000), 463. ISSN: 10871357. DOI: 10.1115/1.1285907.

[52] J. M. Lawrence, V. Neacsu, and S. G. Advani. Modeling the impact of capillary pressure and air entrapment on fiber tow saturation during resin infusion in LCM. *Composites Part A: Applied Science and Manufacturing*. Special Issue: 15th French National Conference on Composites - JNC15 **40**.8 (Aug. 2009), 1053–1064. ISSN: 1359-835X. DOI: 10.1016/j.compositesa.2009.04.013.

[53] M. Li, S. Wang, Y. Gu, Z. Zhang, Y. Li, and K. Potter. Dynamic capillary impact on longitudinal micro-flow in vacuum assisted impregnation and the unsaturated permeability of inner fiber tows. *Composites Science and Technology* **70**.11 (Oct. 2010), 1628–1636. ISSN: 0266-3538. DOI: 10.1016/j.compscitech.2010.06.004.

[54] J. García, L. Gascón, F. Chinesta, E. Ruiz, and F. Trochu. An efficient solver of the saturation equation in liquid composite molding processes. *International journal of material forming* **3**.2 (2010), 1295–1302.

[55] M. Yeager, W. R. Hwang, and S. G. Advani. Prediction of capillary pressure for resin flow between fibers. *Composites Science and Technology* **126** (Apr. 2016), 130–138. ISSN: 0266-3538. DOI: 10.1016/j.compscitech.2016.02.014.

[56] K. Andriamananjara, N. Moulin, J. Bruchon, P.-J. Liotier, and S. Drapier. Numerical modeling of local capillary effects in porous media as a pressure discontinuity acting on the interface of a transient bi-fluid flow. *Int J Mater Form* (Sept. 17, 2018). ISSN: 1960-6214. DOI: 10.1007/s12289-018-1442-3.

[57] W Ehlers, T Graf, and M Ammann. Deformation and localization analysis of partially saturated soil. *Computer methods in applied mechanics and engineering* **193**.27-29 (2004), 2885–2910.

[58] R. Larsson, M. Rouhi, and M. Wysocki. Free surface flow and preform deformation in composites manufacturing based on porous media theory. *European Journal of Mechanics - A/Solids* **31**.1 (Jan. 2012), 1–12. ISSN: 0997-7538. DOI: 10.1016/j.euromechsol.2011.06.015.

[59] M. S. Rouhi, M. Wysocki, and R. Larsson. Modeling of coupled dual-scale flow deformation processes in composites manufacturing. *Composites Part A: Applied Science and Manufacturing* **46** (Mar. 2013), 108–116. ISSN: 1359-835X. DOI: 10.1016/j.compositesa.2012.11.002.

[60] S. A. Niaki, A. Forghani, R. Vaziri, and A. Poursartip. A three-phase integrated flow-stress model for processing of composites. *Mechanics of Materials* **117** (Feb. 2018), 152–164. ISSN: 0167-6636. DOI: 10.1016/j.mechmat.2017.10.012.

[61] S. Toll. Packing mechanics of fiber reinforcements. en. *Polymer Engineering & Science* **38**.8 (Aug. 1998), 1337–1350. ISSN: 1548-2634. DOI: 10.1002/pen.10304.

[62] R. Mathur, S. G. Advani, J. Gillespie Jr, and B. Fink. A Closed Form Solution for Flow During the Vacuum Assisted Resin Transfer Molding Process. *Journal of Manufacturing Science and Engineering* **122** (2000), 463–475.

[63] M. Li and C. L. Tucker. Modeling and simulation of two-dimensional consolidation for thermoset matrix composites. *Composites Part A: Applied Science and Manufacturing* **33**.6 (June 2002), 877–892. ISSN: 1359-835X. DOI: 10.1016/S1359-835X(02)00017-9.

[64] J. Larsson and R. Larsson. Non-linear analysis of nearly saturated porous media: theoretical and numerical formulation. *Computer Methods in Applied Mechanics and Engineering* **191**.36 (Aug. 2002), 3885–3907. ISSN: 0045-7825. DOI: 10.1016/S0045-7825(02)00333-X.

[65] N. C. Correia, F. Robitaille, A. C. Long, C. D. Rudd, P. Simacek, and S. G. Advani. Use of resin transfer molding simulation to predict flow, saturation, and compaction in the VARTM process. *Journal of fluids engineering* **126**.2 (2004), 210–215.

[66] M. Wysocki, R. Larsson, and S. Toll. Hydrostatic consolidation of commingled fibre composites. *Composites Science and Technology* **65**.10 (Aug. 2005), 1507–1519. ISSN: 0266-3538. DOI: 10.1016/j.compscitech.2005.01.002.

[67] J. Li, C. Zhang, R. Liang, B. Wang, and S. Walsh. Modeling and analysis of thickness gradient and variations in vacuum-assisted resin transfer molding process. *Polym Compos* **29**.5 (May 2008), 473–482. ISSN: 1548-0569. DOI: 10.1002/pc.20439.

[68] M. Wysocki, L. E. Asp, S. Toll, and R. Larsson. Two phase continuum modelling of composites consolidation. *Plastics, Rubber and Composites* **38**.2-4 (May 2009), 93–97. ISSN: 1465-8011. DOI: 10.1179/174328909X387856.

[69] M. Wysocki, S. Toll, R. Larsson, and L. E. Asp. Anisotropic and tension–compression asymmetric model for composites consolidation. *Composites Part A: Applied Science and Manufacturing* **41**.2 (Feb. 2010), 284–294. ISSN: 1359-835X. DOI: 10.1016/j.compositesa.2009.10.016.

[70] F. LeBel, A. E. Fanaei, E. Ruiz, and F. Trochu. Prediction of optimal flow front velocity to minimize void formation in dual scale fibrous reinforcements. *Int J Mater Form* **7**.1 (Mar. 2014), 93–116. ISSN: 1960-6206, 1960-6214. DOI: 10.1007/s12289-012-1111-x.

[71] D. Wu, R. Larsson, and M. S. Rouhi. Modeling and Experimental Validation of the VARTM Process for Thin-Walled Preforms. en. *Polymers* **11**.12 (Dec. 2019), 2003. DOI: 10.3390/polym11122003.

[72] D. Wu and R. Larsson. A shell model for resin flow and preform deformation in thin-walled composite manufacturing processes. en. *Int J Mater Form* (Dec. 2019). ISSN: 1960-6214. DOI: 10.1007/s12289-019-01517-z.

[73] M. R. Kamal and S. Sourour. Kinetics and thermal characterization of thermoset cure. en. *Polymer Engineering & Science* **13**.1 (1973), 59–64. ISSN: 1548-2634. DOI: 10.1002/pen.760130110.

[74] T. A. Bogetti and J. W. Gillespie. Process-Induced Stress and Deformation in Thick-Section Thermoset Composite Laminates. en. *Journal of Composite Materials* **26**.5 (Mar. 1992), 626–660. ISSN: 0021-9983. DOI: 10.1177/002199839202600502.

[75] Z.-S. Guo, S. Du, and B. Zhang. Temperature field of thick thermoset composite laminates during cure process. en. *Composites Science and Technology*. JNC13-AMAC-Strasbourg **65**.3 (Mar. 2005), 517–523. ISSN: 0266-3538. DOI: 10.1016/j.compscitech.2004.07.015.

[76] E. Ruiz and F. Trochu. Numerical analysis of cure temperature and internal stresses in thin and thick RTM parts. en. *Composites Part A: Applied Science and Manufacturing* **36**.6 (June 2005), 806–826. ISSN: 1359-835X. DOI: 10.1016/j.compositesa.2004.10.021.

[77] C. Garschke, P. P. Parlevliet, C. Weimer, and B. L. Fox. Cure kinetics and viscosity modelling of a high-performance epoxy resin film. en. *Polymer Testing* **32**.1 (Feb. 2013), 150–157. ISSN: 0142-9418. DOI: 10.1016/j.polymertesting.2012.09.011.

[78] M. Stanko and M. Stommel. Kinetic Prediction of Fast Curing Polyurethane Resins by Model-Free Isoconversional Methods. en. *Polymers* **10**.7 (July 2018), 698. DOI: 10.3390/polym10070698.

[79] Q. Tao, G. Pinter, T. Antretter, T. Krivec, and P. Fuchs. Model free kinetics coupled with finite element method for curing simulation of thermosetting epoxy resins. en. *Journal of Applied Polymer Science* **135**.27 (2018), 46408. ISSN: 1097-4628. DOI: 10.1002/app.46408.

[80] M. Benavente, L. Marcin, A. Courtois, M. Lévesque, and E. Ruiz. Numerical analysis of viscoelastic process-induced residual distortions during manufacturing and post-curing. en. *Composites Part A: Applied Science and Manufacturing* **107** (Apr. 2018), 205–216. ISSN: 1359-835X. DOI: 10.1016/j.compositesa.2018.01.005.

[81] P. Maji and S. Neogi. Development of kinetics sub-model of cyanate ester-based prepregs for autoclave molding process simulation. *High Temperature Materials and Processes* **37**.8 (2018), 769–776. ISSN: 0334-6455. DOI: 10.1515/htmp-2017-0039.

[82] A. Dong, Y. Zhao, X. Zhao, and Q. Yu. Cure Cycle Optimization of Rapidly Cured Out-Of-Autoclave Composites. en. *Materials* **11**.3 (Mar. 2018), 421. DOI: 10.3390/ma11030421.

[83] S.-S. Hwang, S. Y. Park, G.-C. Kwon, and W. J. Choi. Cure kinetics and viscosity modeling for the optimization of cure cycles in a vacuum-bag-only prepreg process. en. *Int J Adv Manuf Technol* **99**.9 (Dec. 2018), 2743–2753. ISSN: 1433-3015. DOI: 10.1007/s00170-018-2467-y.

[84] S. Y. Park, C. H. Choi, W. J. Choi, and S. S. Hwang. A Comparison of the Properties of Carbon Fiber Epoxy Composites Produced by Non-autoclave with Vacuum Bag Only Prepreg and Autoclave Process. en. *Appl Compos Mater* **26**.1 (Feb. 2019), 187–204. ISSN: 1573-4897. DOI: 10.1007/s10443-018-9688-y.

[85] A. Muc, P. Romanowicz, and M. Chwał. Description of the Resin Curing Process—Formulation and Optimization. en. *Polymers* **11**.1 (Jan. 2019), 127. DOI: 10.3390/polym11010127.

[86] J. M. Castro and C. W. Macosko. Studies of mold filling and curing in the reaction injection molding process. en. *AIChE Journal* **28**.2 (1982), 250–260. ISSN: 1547-5905. DOI: 10.1002/aic.690280213.

[87] M. Henne, C. Breyer, M. Niedermeier, and P. Ermanni. A new kinetic and viscosity model for liquid composite molding simulations in an industrial environment. en. *Polymer Composites* **25**.3 (2004), 255–269. ISSN: 1548-0569. DOI: 10.1002/pc.20020.

[88] P. I. Karkanas and I. K. Partridge. Cure modeling and monitoring of epoxy/amine resin systems. II. Network formation and chemoviscosity modeling. en. *Journal of Applied Polymer Science* **77**.10 (2000), 2178–2188. ISSN: 1097-4628. DOI: 10.1002/1097-4628(20000906)77:10<2178::AID-APP11>3.0.CO;2-0.

[89] K. R. R. Pandiyan and S. Neogi. Viscosity modeling of a medium reactive unsaturated polyester resin used for liquid composite molding process. en. *Journal of Applied Polymer Science* **125**.2 (2012), 1400–1408. ISSN: 1097-4628. DOI: 10.1002/app.35447.

[90] H. Wei, H. Liming, M. Zhongliang, and G. Yanlia. The kinetic and viscosity analysis of glycidyl azide polymer spherical propellant. en. *J Therm Anal Calorim* **124**.2 (May 2016), 943–950. ISSN: 1588-2926. DOI: 10.1007/s10973-015-5225-5.

[91] H. Li and B. Zhang. Improved models of viscosity and relaxation modulus for epoxy resin during cure. en. *Polymer Engineering & Science* **56**.6 (2016), 617–621. ISSN: 1548-2634. DOI: 10.1002/pen.24286.

[92] R. Geissberger, J. Maldonado, N. Bahamonde, A. Keller, C. Dransfeld, and K. Masania. Rheological modelling of thermoset composite processing. en. *Composites Part B: Engineering* **124** (Sept. 2017), 182–189. ISSN: 1359-8368. DOI: 10.1016/j.compositesb.2017.05.040.

[93] T. Zhang, Y. Zhao, and B. Zhang. A method based on the time–temperature superposition principle to predict pressurization time in compression molding. en. *Journal of Applied Polymer Science* **135**.36 (2018), 46664. ISSN: 1097-4628. DOI: 10.1002/app.46664.

[94] M. Grujicic, K. M. Chittajallu, and S. Walsh. Non-isothermal preform infiltration during the vacuum-assisted resin transfer molding (VARTM) process. en. *Applied Surface Science* **245**.1 (May 2005), 51–64. ISSN: 0169-4332. DOI: 10.1016/j.apsusc.2004.09.123.

[95] P. Celle, S. Drapier, and J.-M. Bergheau. Numerical modelling of liquid infusion into fibrous media undergoing compaction. en. *European Journal of Mechanics - A/Solids* **27**.4 (July 2008), 647–661. ISSN: 0997-7538. DOI: 10.1016/j.euromechsol.2007.11.002.

[96] F. Shi and X. Dong. 3D numerical simulation of filling and curing processes in non-isothermal RTM process cycle. en. *Finite Elements in Analysis and Design* **47**.7 (July 2011), 764–770. ISSN: 0168-874X. DOI: 10.1016/j.finel.2011.02.007.

[97] L. Ma, S. R. Athreya, R. Mehta, D. Barpanda, and A. Shafi. Numerical modeling and experimental validation of nonisothermal resin infusion and cure processes in large composites: en. *Journal of Reinforced Plastics and Composites* (Feb. 2017). DOI: 10.1177/0731684417691673.

[98] A. Keller, C. Dransfeld, and K. Masania. Flow and heat transfer during compression resin transfer moulding of highly reactive epoxies. en. *Composites Part B: Engineering* **153** (Nov. 2018), 167–175. ISSN: 1359-8368. DOI: 10.1016/j.compositesb.2018.07.041.

[99] N. Burdine. Relative Permeability Calculations From Pore Size Distribution Data. en. *Journal of Petroleum Technology* **5**.03 (Mar. 1953), 71–78. ISSN: 0149-2136. DOI: 10.2118/225-G.

[100] T. S Lundström. The permeability of non-crimp stitched fabrics. *Composites Part A: Applied Science and Manufacturing* **31**.12 (Dec. 2000), 1345–1353. ISSN: 1359-835X. DOI: 10.1016/S1359-835X(00)00037-3.